ELSEVIER

Energetic electron dynamics near Callisto

Lucas Liuzzo [a,b,*], Sven Simon [a], Leonardo Regoli [c]

[a] *School of Earth and Atmospheric Sciences, Georgia Institute of Technology, Atlanta, GA, USA*
[b] *Now at: Space Sciences Laboratory, University of California, Berkeley, CA, USA*
[c] *Department of Climate and Space Sciences and Engineering, University of Michigan, Ann Arbor, MI, USA*

ABSTRACT

We examine the dynamics of energetic magnetospheric electrons exposed to the highly perturbed and asymmetric plasma environment of Jupiter's moon Callisto. The interaction of the (nearly) corotating magnetospheric plasma with Callisto's ionosphere and induced dipole locally generates intense electromagnetic pileup and draping signatures which vary as a function of the moon's distance to the center of Jupiter's magnetospheric current sheet. In our study, these field perturbations are represented using output from the AIKEF hybrid (kinetic ions, fluid electrons) model of Callisto's interaction with the corotating plasma. In order to constrain the influence of Callisto's variable electromagnetic environment on the dynamics of energetic electrons, we trace the trajectories of more than 6.7 million test particles as they travel through a distinct configuration of the locally perturbed fields. We present spatially resolved maps that display the accessibility of Callisto to electrons at energies E between 10^1 keV $\leq E \leq 10^5$ keV for multiple sets of these perturbed fields, corresponding to select distances of the moon to the center of the Jovian current sheet. The electromagnetic field perturbations near Callisto play a crucial role in generating inhomogeneous precipitation of energetic electrons onto the top of the moon's atmosphere. In particular, Callisto's Jupiter-facing and Jupiter-averted hemispheres are partially protected from energetic electron precipitation: when located far above or below the center of Jupiter's current sheet, Callisto's induced dipole shields the apices of these hemispheres, whereas near the center of the sheet, strong field line draping protects these regions. In contrast to this, the apex of Callisto's trailing hemisphere is exposed to intense energetic electron precipitation at any distance to the center of the Jovian current sheet. We also present maps of energetic electron accessibility during the Galileo C3, C9, and C10 flybys, and calculate the intensity of energetic electron flux onto multiple locations at the top of Callisto's atmosphere. These non-uniform electron fluxes likely cause inhomogeneous ionization of Callisto's atmosphere and may even contribute to irregular erosion of the surface. This paper is a companion to Liuzzo et al. (2019), who studied the dynamics of energetic ions near Callisto.

1. Introduction

Callisto (radius $R_C = 2,410$ km) is the second-largest moon of Jupiter and the third-largest in the solar system. Models of Callisto's interior suggest that it is only weakly differentiated (Kuskov and Kronrod, 2005), with a subsurface liquid layer sustained by radiogenic heating (Mueller and McKinnon, 1988). Due to the 9.6° tilt between Jupiter's magnetic and rotational axes, the magnetospheric field near Callisto's orbit varies periodically on a time scale determined by Jupiter's synodic rotation of 10.18 h (Seufert et al., 2011). Thus, currents are induced within Callisto's subsurface ocean (Khurana et al., 1998; Kivelson et al., 1999) and conducting ionosphere (Hartkorn and Saur, 2017), manifesting outside of the moon as a secondary, quasi-dipolar field with a time-varying

magnetic moment (Zimmer et al., 2000). Magnetic signatures associated with this induced field have been observed during multiple Callisto flybys of the Galileo spacecraft (e.g., Khurana et al. (1998); Kivelson et al. (1999); Liuzzo et al. (2016)).

Callisto orbits its parent planet at a distance of $26.3R_J$ (radius of Jupiter $R_J = 71,492$ km), and is therefore always contained well within the Jovian magnetosphere (Joy et al., 2002). Throughout its orbit, Callisto is continuously exposed to two populations of Jovian magnetospheric plasma: the "thermal" and the "energetic" populations. The "thermal" plasma near the moon is mainly comprised of H^+ and O^+ ions, as well as electrons, with energies $E \leq 10$ keV (Belcher, 1983) and with ion and electron number densities n that range from $0.01\,cm^{-3} \leq n \leq 0.7\,cm^{-3}$ (Kivelson et al., 2004). This population nearly

---

corotates with Jupiter and impinges onto Callisto's ramside (orbital trailing) hemisphere, continually overtaking the moon at a relative velocity of approximately 192 km/s. Callisto's atmosphere (e.g., Carlson (1999); Cunningham et al. (2015)), ionosphere (e.g., Kliore et al. (2002); Hartkorn et al. (2017)), and induced field represent obstacles to this thermal plasma population. The magnetospheric field, frozen-in to the thermal plasma, compresses the moon's induced dipole as it piles up at Callisto's ramside and drapes around the obstacle (Liuzzo et al., 2016, 2017). Plasma from Callisto's ionosphere, predominately generated by solar ultraviolet ionization (and to a lesser degree, by electron impacts), experiences the ambient electromagnetic fields and is convected toward downstream by the $\mathbf{E} \times \mathbf{B}$ drift. This generates large-scale asymmetries in the plasma flow pattern: ionospheric ions possess gyroradii that can be up to 10 times larger than Callisto's radius (Kivelson et al., 2004). Thus, the resulting electromagnetic perturbations near the moon are highly asymmetric with respect to the direction of the convective electric field (Liuzzo et al., 2015).

At larger distances to Callisto, currents generated locally by the thermal plasma interaction are closed by currents that flow along the characteristics of Callisto's Alfvén wings (Neubauer, 1980, 1998). This system of non-linear standing Alfvén waves electromagnetically connects the moon to Jupiter's polar ionosphere. The visible manifestation of this thermal plasma interaction has recently been detected as Callisto's auroral footprint in Hubble Space Telescope observations of Jupiter's polar ionosphere (Bhattacharyya et al., 2017).

Due to the tilt between the Jovian magnetic and rotational axes, Callisto's interaction with the thermal magnetospheric plasma population is highly variable as a function of System III longitude λ_{III} (i.e., as the moon passes in and out of Jupiter's magnetospheric current sheet over half of a synodic rotation). At maximum distances h_{cs} of Callisto to the center of the magnetospheric current sheet (at approximately $4.5R_J$, near $\lambda_{\mathrm{III}} = 20°$ and $\lambda_{\mathrm{III}} = 200°$), the moon's induced dipole field dominates the weak magnetic perturbations generated by deflection of the dilute upstream plasma (e.g., Zimmer et al. (2000); Liuzzo et al. (2015)). At intermediate distances to the center of Jupiter's current sheet, the magnetic perturbations associated with a stronger plasma interaction partially obscure the moon's induced dipole (Liuzzo et al., 2018). Nonetheless, magnetic signatures of Callisto's unaltered induced field are still visible within a quasi-dipolar "core region" located in the moon's wake below altitudes of $1R_C$ (Liuzzo et al., 2016). When Callisto is located close to the center of Jupiter's current sheet (i.e., with $h_{\mathrm{cs}} \approx 0$, occurring near $\lambda_{\mathrm{III}} = 110°$ and $\lambda_{\mathrm{III}} = 290°$), Callisto's induced field nearly vanishes and the magnetic perturbations near the moon are generated by the interaction between the thermal magnetospheric plasma and Callisto's atmosphere/ionosphere alone (Liuzzo et al., 2015, 2017).

The "energetic" plasma population near Callisto's orbit is comprised of electrons as well as hydrogen, oxygen, and sulfur ions with energies $E \geq 10$ keV (Cooper et al., 2001). These particles drift through Jupiter's magnetosphere azimuthally and are trapped within the magnetospheric field as they bounce between the planet's magnetic poles. The number densities of the energetic ions and electrons near Callisto are below $n \approx 0.01$ cm^{-3} (Mauk et al., 2004). Thus, these particles make only a minor contribution to currents near Callisto and do not noticeably alter the electromagnetic fields generated by the moon's interaction with the thermal magnetospheric plasma (e.g., Zimmer et al. (2000); Liuzzo et al. (2015, 2016)). Hence, the energetic population can be treated as test-particles exposed to a pre-defined electromagnetic field configuration (Liuzzo et al., 2019).

Multiple studies have used a combination of data from the Galileo spacecraft's *Energetic Particle Detector* (EPD, Williams et al. (1992)) and modeling techniques to investigate the dynamics of the Jovian energetic particle population near the icy Galilean moons. The pronounced leading/trailing hemispherical asymmetry of Europa's surface coloring (Johnson et al., 1983; McEwen, 1986) has been explained by preferential access of energetic electrons to its orbital trailing hemisphere (Paranicas et al., 2001). Nordheim et al. (2018) have recently identified a strong

latitudinal/longitudinal asymmetry in the precipitation patterns of energetic particles and in the associated radiation dosage into Europa's surface. Ip et al. (1998) used EPD data to constrain the sputtering rate of Europa's surface, and precipitation by energetic ions was found to be a substantial agent for the generation of the moon's tenuous exosphere (e.g., Plainaki et al. (2013); Cassidy et al. (2013)). Dalton et al. (2013) and Vorburger and Wurz (2018) have also shown that energetic electrons make non-negligible contributions to exospheric genesis at Europa. Paranicas et al. (2000) have presented observational evidence of the strong effect that Europa's perturbed electromagnetic environment has on the energetic electron population near the moon. These authors suggested that pileup of the magnetospheric field at Europa's ramside was responsible for the observed "dropout" signatures in energetic electron count rates measured by EPD during several close Galileo flybys.

At Ganymede, Ip et al. (1997) found that precipitation of energetic ions onto the moon's surface significantly contributes to generation of its exosphere, while Cooper et al. (2001) have shown that the moon's intrinsic magnetic field partially shields the surface from energetic ion bombardment. Studies by Eviatar et al. (2001) and McGrath et al. (2013) have shown that acceleration of energetic particles and subsequent precipitation into Ganymede's exosphere generate persistent ultraviolet aurorae, as observed by, e.g., Hall et al. (1998) and Feldman et al. (2000) using the Hubble Space Telescope. Fatemi et al. (2016), and recently Poppe et al. (2018), have investigated the influence of Ganymede's thermal plasma interaction on the deformation of the moon's permanent dipole field and on the dynamics of energetic ions. These authors demonstrated that the resulting electromagnetic perturbations generate energetic particle precipitation patterns that coincide with the moon's observed high-latitude surface brightness patterns. Overall, these findings also agree with the results of, e.g., Roussos et al. (2012), Krupp et al. (2013), Kotova et al. (2015) and Regoli et al. (2016), who have emphasized the drastic influence of the thermal plasma interaction on energetic particle precipitation at Saturn's moons Dione, Rhea, and Titan.

Despite their important role in generating the exospheres and surface features at various icy moons throughout the solar system, energetic particle dynamics and their response to the locally perturbed electromagnetic fields near Callisto have remained vastly under-constrained. Using Galileo EPD data, Cooper et al. (2001) investigated the energetic particle irradiation of Callisto's surface. By converting measured energy spectra for energetic electrons as well as H$^+$, O^{2+}, and S^{3+} ions into surface fluxes, these authors found that the electron energy flux is nearly twice as large as the combined ion energy flux. However, Cooper et al. (2001) did not consider the influence of the electromagnetic perturbations near the moon on the dynamics of these energetic particles. Instead, they treated Callisto as an electromagnetically inert object embedded in a constant magnetic field (i.e., without its induced field), and did not account for any perturbations generated by plasma currents. These authors also assumed an omnidirectional flux of energetic particles spread uniformly across the moon's surface.

However, Liuzzo et al. (2019) have recently shown that the accessibility of Callisto's surface to energetic ions is decidedly *not* uniform. By combining a test particle model for energetic H$^+$, O^{2+}, and S^{3+} ions with a hybrid model of the electromagnetic field perturbations, these authors found that the interaction of the thermal plasma with Callisto's ionosphere and induced dipole leaves distinct imprints on the precipitation patterns of energetic ions. In particular, Liuzzo et al. (2019) found that energetic ion deflection around Callisto's ramside magnetic pileup barrier generates a gap in ion precipitation onto the moon's trailing hemisphere, whereas Callisto's induced magnetic field generates a characteristic ring-like depletion in the wakeside precipitation pattern. Liuzzo et al. (2019) also found a strong variability in the precipitation patterns of energetic ions as a function of Callisto's distance h_{cs} to the center of the Jovian magnetospheric current sheet. At large distances, these authors found a distinct north/south asymmetry in the precipitation pattern, whereas closer to the center of the sheet, ion precipitation was longitudinally inhomogeneous.

Although the contribution of energetic electrons to sputtering of Callisto's surface as well as genesis and ionization of its atmosphere may be substantial (e.g., Spencer (1987); Vorburger et al. (2015)), and despite the observed disparities in the coloring and composition of its surface (e.g., Hibbitts et al. (2000); Hendrix and Johnson (2008)), the spatial pattern of energetic electron precipitation onto Callisto has not yet been constrained by any study. Besides, although energetic *ion* dynamics are strongly affected by the perturbed electromagnetic fields near Callisto (Liuzzo et al., 2019), no study has considered the influence of the moon's thermal plasma interaction on the dynamics and precipitation patterns of energetic *electrons* at different h_{cs} values. Therefore, this study will systematically constrain the effect of Callisto's interaction with the thermal plasma on the dynamics of energetic electrons near the moon.

Our study is structured as follows: Section 2.1 describes the hybrid model used to represent the electromagnetic field perturbations near Callisto. A discussion on the key features of Callisto's electromagnetic environment for four scenarios representing various distances h_{cs} to the center of Jupiter's magnetospheric current sheet is also included in this section. The test particle model applied to study the dynamics of energetic electrons near the moon is described in Section 2.2. Sections 3.1–3.4 present maps of energetic electron precipitation for each of the four thermal plasma interaction scenarios. These findings are then applied in Section 4 to understand the energetic electron precipitation patterns onto Callisto during the C3, C9, and C10 Galileo flybys. Conclusions of this study are presented in Section 5.

2. Modeling Callisto's plasma environment

2.1. Hybrid simulations of Callisto's thermal plasma interaction

Any simulation of Callisto's thermal plasma and electromagnetic environment must treat ions as kinetic in order to accurately resolve their large gyroradii and the associated asymmetries in the plasma flow patterns and field perturbations near the moon (e.g., Liuzzo et al. (2015)). Hence, to investigate Callisto's interaction with its thermal magnetospheric environment, we use the *Adaptive Ion-Kinetic, Electron-Fluid* (AIKEF) hybrid model (Müller et al., 2011). AIKEF has already been extensively applied to Callisto in several preceding studies (Liuzzo et al., 2015, 2016, 2017, 2018, 2019). Within the model, Callisto's O_2 and CO_2 atmosphere is represented using a barometric law with a superimposed ramside/wakeside asymmetry, consistent with observations (see, e.g., Carlson (1999); Cunningham et al. (2015)). This atmosphere is ionized via a combination of solar ultraviolet ionization, electron impacts, and charge exchange with the upstream plasma. Callisto's induced dipole is represented by a static magnetic moment M_{ind} centered at the moon (Zimmer et al., 2000; Seufert et al., 2011). For further details on the model, the reader is referred to any of our five aforementioned studies.

In analogy to Liuzzo et al. (2019), Section 3 of our study will focus on Callisto's interaction with the thermal magnetospheric plasma during four distinct scenarios. Each of these setups corresponds to idealized conditions at a specific distance h_{cs} of Callisto to the center of Jupiter's current sheet (see Table 1 for more details). The vector quantities in Table 1 are displayed in CphiO coordinates. In this Callisto-centered Cartesian system, unit vector $\hat{x}$ is aligned with the corotational flow direction, $\hat{y}$ points toward Jupiter, and unit vector $\hat{z}$ completes the right-handed set. In order to facilitate comparison between the dynamics of energetic electrons and ions, the four thermal plasma interaction scenarios considered in Section 3 are *identical* to those used by Liuzzo et al. (2019). These four idealized scenarios form the basis for our subsequent study of energetic electron dynamics and precipitation during the C3, C9, and C10 Galileo flybys of Callisto.

The setups of the four idealized interaction scenarios are discussed in detail by Liuzzo et al. (2019), and are only summarized here:

Run #1: The first thermal plasma interaction scenario corresponds to Callisto located at maximum distance h_{cs} to the center of the Jovian

Table 1

Hybrid simulation parameters of Runs #1–#4 (see also Liuzzo et al. (2019)). Values used for the magnetospheric background field ($\mathbf{B}_0$), bulk velocity ($\mathbf{u}_0$), ion mass (m_0), and number density (n_0), as well as the plasma beta (β) and the Mach numbers (Alfvénic M_A, magnetosonic M_{MS}, and sonic M_S) are within the range those observed near Callisto's orbit (see, e.g., Kivelson et al. (2004)). The magnitude and orientation of Callisto's induced magnetic moment $\mathbf{M}_{ind}$ are consistent with previous studies (e.g., Zimmer et al. (2000); Liuzzo et al. (2016)).

	Run #1	Run #2	Run #3	Run #4
Plasma interaction?	No	Yes	Yes	Yes
Ionosphere?	No	No	Yes	Yes
Induced dipole?	Yes	Yes	No	Yes
$\mathbf{M}_{ind}$ ($\cdot 10^{18}$ Am^2)	$+2.35\hat{y}$	$+2.35\hat{y}$	N/A	$+2.35\hat{y}$
$\mathbf{B}_0$ (nT)	$-33.58\hat{y}$	$-33.58\hat{y}$	$-33.58\hat{y}$	$-33.58\hat{y}$
$\mathbf{u}_0$ (km/s)	$+192\hat{x}$	$+192\hat{x}$	$+192\hat{x}$	$+192\hat{x}$
$\mathbf{E}_0 = -\mathbf{u}_0 \times \mathbf{B}_0$ (mV/m)	$+6.4\hat{z}$	$+6.4\hat{z}$	$+6.4\hat{z}$	$+6.4\hat{z}$
m_0 (amu)	N/A	16 (O$^+$)	16 (O$^+$)	16 (O$^+$)
n_0 (cm^{-3})	N/A	0.58	0.58	0.58
β	N/A	0.53	0.53	0.53
M_A	N/A	0.8	0.8	0.8
M_{MS}	N/A	0.6	0.6	0.6
M_S	N/A	1.1	1.1	1.1
AIKEF domain (R_C)	N/A	$-15 \leq x,y,$ $z \leq 15$	$-15 \leq x,y,$ $z \leq 15$	$-15 \leq x,y,$ $z \leq 15$
Max. AIKEF resolution (R_C)	N/A	0.05	0.05	0.05

current sheet. This electromagnetic field configuration is used to determine the "baseline" behavior of energetic electrons near Callisto, and is represented by the superposition of Callisto's induced dipole field with the magnetospheric background field. This scenario does *not* consider any electromagnetic perturbations generated by Callisto's interaction with the thermal magnetospheric plasma. Hence, Run #1 uses an undisturbed convective electric field ($\mathbf{E}_0 = -\mathbf{u}_0 \times \mathbf{B}$, where $\mathbf{B}$ is the superposition of the background field with Callisto's induced field and $\mathbf{u}_0$ is the undisturbed bulk velocity of the thermal plasma).

Run #2: The second thermal plasma interaction scenario occurs when Callisto is located at large distances to the center of the Jovian magnetospheric current sheet, but for a stronger interaction with upstream thermal plasma. At these large h_{cs} values, the electromagnetic field perturbations near Callisto are mainly generated by the dipole-magnetosphere interaction (Zimmer et al., 2000), so Run #2 does not include mass-loading from the moon's ionosphere. Such an interaction was observed during, e.g., the C3 and C9 Galileo flybys of Callisto (Liuzzo et al., 2015).

Run #3: The third scenario is representative of Callisto located near the center of the Jovian magnetospheric current sheet. At these small h_{cs} values, Callisto's induced dipole nearly vanishes (Zimmer et al., 2000), and the electromagnetic perturbations in the model are generated by the ionosphere-magnetosphere interaction alone (Liuzzo et al., 2015). Similar conditions were observed during the Galileo C23 flyby (Liuzzo et al., 2017).
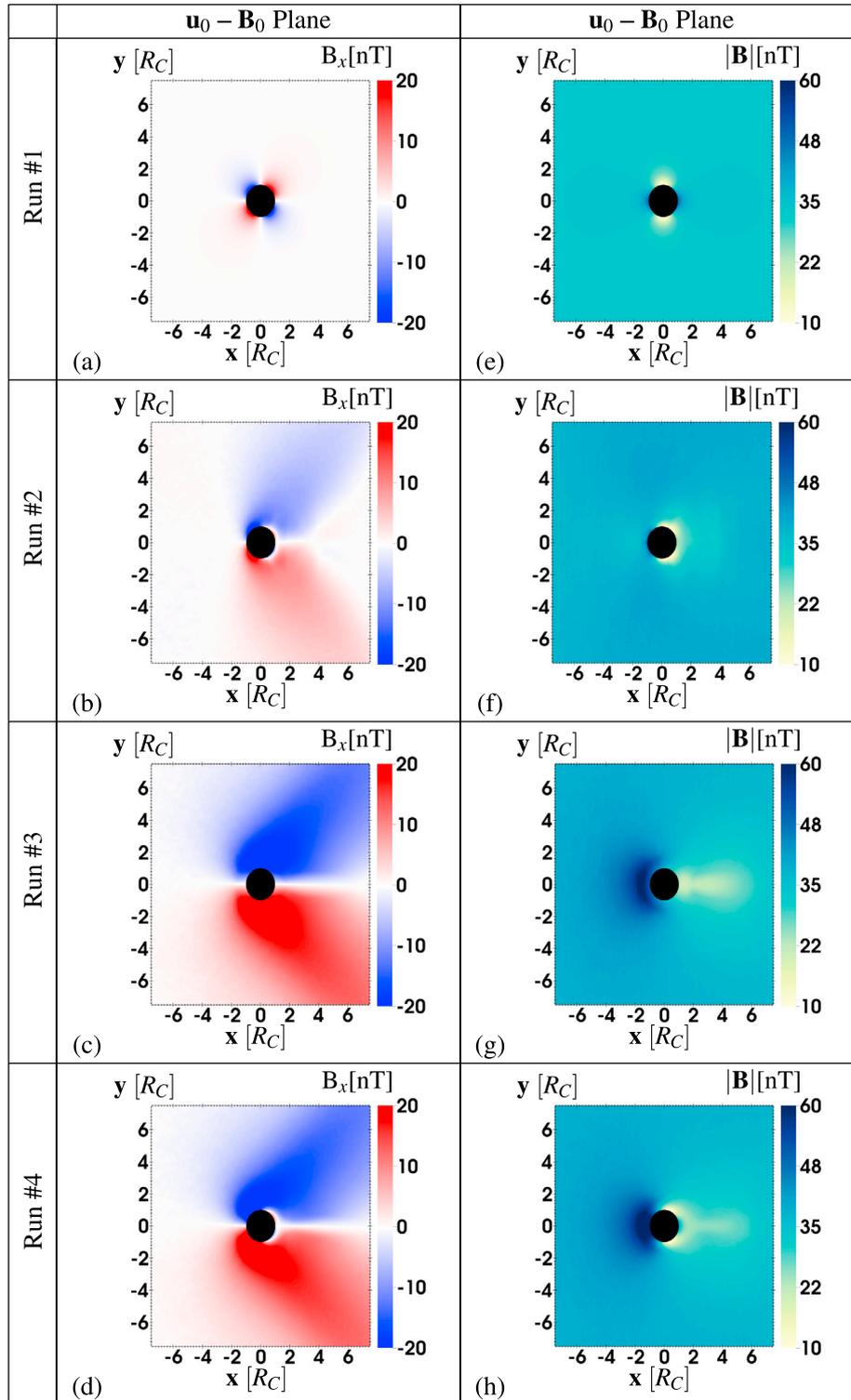
Run #4: The fourth thermal plasma interaction scenario corresponds to those System III longitudes where Callisto is located at intermediate distances to the center of Jupiter's magnetospheric current sheet. In these cases, the electromagnetic perturbations near Callisto are generated by a non-linear coupling of the dipole-magnetosphere and the ionosphere-magnetosphere interactions (represented, in isolation, by Runs #2 and #3, respectively). Thus, the perturbations in Run #4 include contributions from Callisto's induced dipolar field *and* mass-loading from its ionosphere. This scenario is similar to the conditions observed during, e.g., the C10 and C21 Galileo flybys of Callisto (Liuzzo et al., 2016, 2017).

The electromagnetic field perturbations associated with each of the

four idealized scenarios are documented in detail by Liuzzo et al. (2019), so only a brief discussion is provided here. Callisto's magnetic environment for Runs #1–#4 is shown in Fig. 1 in CphiO coordinates. The B_x component of the magnetic field in Callisto's equatorial (x-y) plane is displayed in the first column of Fig. 1 (panels (a)–(d)), whereas the magnitude of the field $|\mathbf{B}|$ in this plane is displayed in the second column (panels (e)–(h)). Discussion of additional plasma quantities is provided by Liuzzo et al. (2019).

The intensity of the B_x perturbations increases from Run #1 to Run #3; i.e., with decreasing h_{cs} values. For maximum distances to the center of the Jovian current sheet (Run #1), panel 1(a) shows the unperturbed "shamrock leaves" in B_x generated by Callisto's induced dipole. Subtle Alfvén wings already form through the weak interaction of the thermal plasma with this dipole (Run #2, see panel 1(b)), whereas the contribution of Callisto's ionosphere to the plasma currents drastically amplifies the B_x perturbations (Run #3 in Fig. 1(c)). Fig. 1(d) shows that, at intermediate h_{cs} values (Run #4), Callisto's induced dipole is compressed at the ramside and completely shrouded by pileup of the magnetospheric

Fig. 1. Magnetic field near Callisto associated with the four thermal plasma interaction scenarios in Table 1: (Run #1) a very weak interaction with Callisto's induced dipole, (Run #2) a stronger plasma interaction with the induced dipole, (Run #3) the plasma interaction with Callisto's ionosphere alone, and (Run #4) the interaction with Callisto's ionosphere *and* induced dipole. The first column (panels (a)–(d)) shows the corotation-aligned magnetic field component B_x in Callisto's equatorial ($z = 0$) plane which contains the background field $\mathbf{B}_0$ and the upstream flow velocity $\mathbf{u}_0$ for the four runs. The second column (panels (e)–(h)) displays the magnitude of the magnetic field $|\mathbf{B}|$ in the moon's equatorial plane. Callisto is represented by the black circle in each panel. The figure has been adapted from Liuzzo et al. (2019).

field. At Callisto's wakeside, however, the unobscured induced field is still discernible within a quasi-dipolar "core region" that is confined close to the moon's surface. Within this narrow region, the orientation of the magnetic field is reversed compared to the orientation within the Alfvén wings: where field line draping generates $B_x < 0$, the induced dipole results in a sliver of $B_x > 0$ close to the moon's surface, and vice versa.

Similarly, the intensity of the ramside magnetic field pileup also increases with decreasing distance to the center of the current sheet. Panel 1(e) shows that the magnetic field $|\mathbf{B}|$ in Run #1 is reduced at Callisto's two "magnetic poles" near $[x = 0, y = \pm 1 R_C]$ and enhanced at Callisto's "magnetic equator" (in this plane, near $[x = \pm 1 R_C, y = 0]$), see also Liuzzo et al. (2017). Weak signatures of field line pileup at Callisto's ramside are visible in Fig. 1(b) at large h_{cs} values, and the regions of reduced $|\mathbf{B}|$ near the "magnetic poles" are slightly shifted toward downstream by the plasma flow. Closer to the center of the magnetospheric current sheet (panels 1(g) and 1(h)), strong pileup occurs and an associated region of reduced magnetic field forms downstream.

To facilitate understanding of energetic electron dynamics at multiple h_{cs} values, these four idealized runs use *identical* properties of the upstream thermal magnetospheric plasma. For each of these scenarios (see Table 1), the magnetospheric background field is oriented along the $-y$-axis, and the upstream plasma flows along the $+x$-axis. This allows for a straightforward comparison between the subsequent test particle simulations of Callisto's energetic electron environment for each electromagnetic field configuration (see Section 3): any differences in the electron precipitation patterns between the four cases must be a result of changes in the electromagnetic field *perturbations* generated by Callisto's thermal plasma interaction, but are *not* a caused by, e.g., a different strength or orientation of the upstream magnetic field.

Understanding the energetic electron precipitation patterns for these four idealized scenarios is necessary to interpret the modeled patterns during the C3, C9, and C10 flybys, where the magnetospheric background field $\mathbf{B}_0$ had three non-zero components and Callisto's induced dipole moment $\mathbf{M}_{ind}$ was inclined against the background field. However, it is still important to recognize that Runs #1–#4 represent idealized snapshots of Callisto's electromagnetic environment. In particular, for Callisto's induced dipole to be absent (as is the case in Run #3, see Table 1), the time-varying component of the magnetospheric background field must vanish. This occurs while Callisto is located close to the center of Jupiter's magnetospheric current sheet, where the orientation of the background field would be mainly along the $-z$-axis (Kivelson et al., 1999). However, aligning the background field southward in Run #3 would merely result in a 90° rotation of the energetic electron precipitation patterns around the x-axis, but this would not otherwise change the patterns nor facilitate understanding of the physical processes responsible for generating them. Thus, the orientation of the background field has been chosen to remain identical between the four idealized runs. For our investigation of energetic electron precipitation during the C3, C9, and C10 flybys, the electromagnetic fields near Callisto have been taken from Liuzzo et al. (2015) for C3 and C9, and Liuzzo et al. (2016) for C10, who used the magnetospheric upstream conditions that achieved the best possible agreement with Galileo observations.

2.2. Test particle simulations of energetic electron dynamics near Callisto

The AIKEF model treats electrons as a massless, charge-neutralizing fluid (Müller et al., 2011). Since the fluid assumption is not fulfilled for gyrating energetic electrons, and since hybrid simulations consider only a *single* electron fluid (i.e., there is no discrimination between thermal and energetic electrons), it is not possible to model the dynamics of energetic electrons using AIKEF. Instead, due to their test particle nature, we study energetic electron dynamics using the established, parallelized, *Galilean Energetics Tracing Model* (GENTOo, Liuzzo et al. (2019)).

The dynamics of an energetic electron with rest mass m and charge $q = -e$ while embedded in an electric field $\mathbf{E}$ and magnetic field $\mathbf{B}$ are governed by the Lorentz force:

$$m \frac{d(\gamma \mathbf{v})}{dt} = q(\mathbf{E} + \mathbf{v} \times \mathbf{B}) \quad . \tag{1}$$

The velocity $\mathbf{v}$ of such an electron is related to its kinetic energy E through

$$E = E_{\text{tot}} - E_0 = (\gamma - 1)mc^2 \quad , \tag{2}$$

with total energy $E_{\text{tot}} = \gamma mc^2$, rest energy $E_0 = mc^2$, and the Lorentz factor

$$\gamma = \frac{1}{\sqrt{1 - \frac{|\mathbf{v}|^2}{c^2}}} \quad . \tag{3}$$

Hence, the velocity of an electron can be expressed as

$$|\mathbf{v}| = c \sqrt{1 - \frac{1}{\left(1 + \frac{E}{mc^2}\right)^2}} \quad . \tag{4}$$

For non-relativistic particles with $\gamma \approx 1$ (i.e., at low energies), equation (4) becomes $|\mathbf{v}| = \sqrt{2E/m}$. In this non-relativistic case, equation (1) can be solved using, e.g., a fourth-order Runge-Kutta integration routine for a value of $\gamma = 1$ (Liuzzo et al., 2019). However, with increasing energy E, the value of γ deviates from 1 and relativistic effects can no longer be neglected. Table 2 shows the value of γ at select energies, as well as the (relativistic) gyroradius $r_g = (\gamma m |\mathbf{v}_\perp|)/(e|\mathbf{B}|)$ of an electron with a velocity $\mathbf{v}_\perp$ perpendicular to the magnetic field. As can be seen, an electron with an energy of 10 keV (i.e., at the lower end of the range of energies studied here) already has a Lorentz factor of $\gamma \approx 1.2$, corresponding to a velocity $|\mathbf{v}| = 0.55c$. Hence, relativistic effects must be considered in evaluation of equation (1). A second-order numerical solution to the relativistic equation of motion has been introduced by Boris (1970) and improved by Vay (2008). The scheme introduced by Vay (2008) (see Section II.B of that work) uses a leapfrog approach to solve equation (1), and is included in GENTOo to investigate the dynamics of energetic electrons near Callisto.

To avoid tracing large numbers of electrons that would never interact with Callisto (and thus, would *not* contribute to precipitation), GENTOo uses a time step $\Delta t < 0$; i.e., electrons of a given energy E are injected near Callisto's surface and traced *backward* in time. A similar *back-tracing* approach has been used to study energetic particle dynamics at, e.g., Ganymede (Cooper et al., 2001; Poppe et al., 2018), Europa (Cassidy et al., 2013; Dalton et al., 2013), and previously for ions at Callisto (Liuzzo et al., 2019).

Callisto's atmosphere has a scale height that is about 1% of the moon's radius (Carlson, 1999). However, it is not feasible for any hybrid model to simultaneously resolve the electromagnetic fields within this atmosphere (with spatial scales on the order of $0.01 R_C$) as well as the large-scale magnetic signatures (e.g., field line draping and pileup) that extend several tens of R_C from the moon. Instead, the hybrid model uses

Table 2
Lorentz factor γ and (relativistic) gyroradius r_g for electrons at select energies E with a pitch angle of $\alpha \approx 90°$ in a magnetic field with magnitude $|\mathbf{B}_0| = 33.58$ nT, as observed during the Galileo C3 flyby of Callisto. Thermal energies are those above the dashed line, where relativistic effects are negligible. Below the dashed line, relativistic effects must be included to accurately represent electron dynamics.

E (keV)	γ	r_g (R_C)
0.1	1.0002	0.0004
1	1.002	0.001
10	1.196	0.004
100	2.957	0.014
1,000	10.78	0.059
10,000	20.57	0.433
100,000	196.7	4.143

an atmospheric scale height that is increased by a factor of 10 while maintaining the observed column density and total gas content of Callisto's atmosphere. Therefore, the electromagnetic fields below approximately $0.1R_C$, and thus energetic electron dynamics below that altitude, are not represented in a quantitatively realistic way. Further details on the model of Callisto's atmosphere can be found in Liuzzo et al. (2015, 2016, 2019). Still, we note that Vorburger et al. (2015) presented evidence that intense sputtering of Callisto's surface may increase the scale height to values well above $0.1R_C$.

Hence, analogous to Liuzzo et al. (2019), this study will investigate energetic particle precipitation onto Callisto's atmosphere at an altitude of $0.1R_C$. We surround Callisto with a spherical starting grid for the energetic electrons that is located at a radial distance of $\tilde{R}_C = 1.1R_C$ to the center of the moon with a resolution of 5° in latitude and 5° in longitude. At each of the nearly 2,600 grid points, electrons of a given velocity $|\mathbf{v}|$ (i.e., at a distinct kinetic energy E within the range 10^1 keV $\leq E \leq 10^5$ keV) are initialized with velocity vectors $\mathbf{v}$ at discrete orientations with respect to the local normal direction and traced *backward* in time. In velocity space, particles are launched at an angular resolution of 5° against the local zenith and 5° in azimuth, yielding approximately 2,600 particles launched from *every point* on the starting grid. Thus, each individual GENTOo simulation calculates the trajectories of $2,600^2 \approx 6.7$ million electrons.

2.3. Boundary conditions for energetic electron dynamics

During its back-tracing through Callisto's perturbed electromagnetic environment, an energetic electron will experience one of two outcomes. The first is that it re-encounters the starting grid, in which case its trajectory is "forbidden." In a forward-tracing approach, this electron would have to travel *through* Callisto's collisional atmosphere, and potentially even through the solid body of the moon itself, in order to reach the point where it was launched in the back-tracing approach. Hence, a "forbidden" particle can *not* contribute to energetic electron precipitation onto the top of the moon's atmosphere.

As long as an electron is located within the AIKEF domain, GENTOo applies trilinear interpolation to obtain the electromagnetic fields at the electron's position using the values defined at the eight adjacent grid nodes of the hybrid simulation. Since the gyroradius of a 10 keV electron is on the order of $10^{-3}R_C$ (see Table 2), electron gyration at the lower energies considered in this study occurs on scales below the resolution of the field data from the hybrid simulation ($0.05R_C$, see Table 1). While the trilinear interpolation method is accurate to first order (Matsumoto and Omura, 1985), the influence of non-linear changes in the fields on scales below the AIKEF cell size are not resolved. Taking into account this finite grid resolution, we adopt the approach of Regoli et al. (2016) for energetic ion dynamics near Titan: we allow for a small excursion (on the order of the AIKEF cell size) of a gyrating electron slightly below the starting grid. Hence, electrons are allowed to travel up to $0.05R_C$ closer to Callisto before their trajectories are considered forbidden; i.e., the hard cutoff for forbidden electrons occurs at an altitude of $1.05R_C$.

We note that at the lowest energies considered in this study (below $E \approx 100$ keV), electron dynamics could likewise be described by tracing the motion of their guiding centers (see, e.g., Roussos et al. (2012); Krupp et al. (2013)). With increasing energy, however, electron gyroradii become larger and exceed $1R_C$ (see Table 2). Thus, using a guiding center approach would no longer be applicable to study their dynamics.

The second outcome that can occur during back-tracing of an energetic electron is that its altitude never drops below the cutoff; i.e., the electron's position $\mathbf{r}(x,y,z) = [x\hat{\mathbf{x}} + y\hat{\mathbf{y}} + z\hat{\mathbf{z}}]$ continuously remains at $|\mathbf{r}| > 1.05R_C$. In this case, GENTOo continues to update the position and velocity of the electron until it leaves the AIKEF simulation domain. As soon as this occurs, a different treatment of the electromagnetic fields is

required to continue tracing the electron.

2.3.1. Bounce motion of energetic electrons near Callisto's orbital position

AIKEF, as with any local plasma interaction model, can only calculate the electromagnetic field perturbations within a box of size $\approx \pm 15R_C$ in each direction, centered at Callisto (see Table 1). At these distances, the field perturbations generated by Callisto have either faded away or are highly localized within the two Alfvén wings extending from the moon. Liuzzo et al. (2019) demonstrated that, if an energetic *ion* leaves Callisto's local environment (in a forward-tracing approach), then travels along a magnetospheric field line toward Jupiter and mirrors, it returns to Callisto's orbit at an azimuthal displacement r_{eq} along the corotation direction x of *at least* $r_{eq} = 11R_C$ downstream of the moon. Hence, such an ion is unable to re-encounter the locally perturbed fields near Callisto and can not impinge onto the moon after returning. For a back-traced energetic *ion* leaving the AIKEF domain, Liuzzo et al. (2019) therefore treated the magnetospheric fields as homogeneous (and equal to their background values from the hybrid simulation, see Table 1). A given energetic ion had a trajectory that was considered "allowed" after it completed multiple gyrations in the homogeneous fields outside of the AIKEF simulation domain. Such "allowed" ions have counterparts in the forward-tracing approach; i.e., they can precipitate onto Callisto and contribute to energy deposition.

In order to determine whether the assumption of homogeneous electromagnetic fields outside of the AIKEF simulation domain is a valid approximation for energetic *electron* dynamics as well, we apply the method introduced in Roederer (1967). The azimuthal displacement r_{eq} of an electron after leaving Callisto's local environment, mirroring, and then returning to the moon's orbit can be calculated from

$$r_{eq} = v_d \frac{\tau_b}{2} \quad . \tag{5}$$

Here, $\tau_b/2$ is the half bounce time of an electron (i.e., the time an electron requires to travel from Callisto, to its mirror point, and back to the moon). The electron's azimuthal drift velocity $\mathbf{v}_d = v_d\hat{\mathbf{x}} = (v_c + v_m)\hat{\mathbf{x}}$ is the sum of its average corotational v_c and magnetic v_m (gradient and curvature) drifts.

The average magnetic drift velocity v_m of an electron as it travels from Callisto's orbital plane to its mirror point and back can be represented as

$$v_m = \frac{mc^2}{qB_0} \frac{(\gamma^2 - 1)}{\gamma} \frac{|\nabla I|}{S_b} \quad , \tag{6}$$

with $B_0 = |\mathbf{B}_0|$ the magnetospheric field strength near the position of Callisto (i.e., the magnitude of the magnetospheric background field in the AIKEF simulations). In this equation, the parameters

$$I = 2 \int_{s_0}^{s_m} \left(1 - \frac{B(s')}{B_m}\right)^{1/2} ds' \tag{7}$$

and

$$S_b = 2 \int_{s_0}^{s_m} \left(1 - \frac{B(s')}{B_m}\right)^{-1/2} ds' \tag{8}$$

are line integrals related to the length of the magnetic field line along which the electron travels, with field magnitude $B(s')$ at each position s' along the Jovian magnetospheric field line (Roederer, 1967). The bounds of the integrals represent the electron's position s_m at its mirror point and its initial/final position s_0 near Callisto. The magnetic field strength at the electron's mirror point is given by $B_m = B_0/\sin^2(\alpha_{eq})$ for an equatorial pitch angle α_{eq}. In our model, the ∇I term in equation (6) is calculated by computing I for a field line located at Callisto (i.e., at an equatorial distance of $26.3R_J$ to Jupiter) and I for a field line located $\delta = 0.5R_C$ farther outside of Callisto's orbit. The resulting magnetic drift velocity was found to be robust against slight changes of the separation δ between the two field lines, so long as $\delta \ll 1R_J$.

Using the electron's half bounce time given by Roederer (1967),

$$\frac{\tau_b}{2} = \frac{S_b}{|\mathbf{v}|} \quad , \tag{9}$$

where $|\mathbf{v}|$ is the velocity of the electron when it leaves the near-Callisto region (here, the AIKEF domain), the azimuthal displacement r_{eq} in equation (5) can then be evaluated. This formalism assumes that $\tau_b/2$ is much shorter than the time scales during which Jupiter's magnetospheric current sheet sweeps over Callisto. Under this assumption, the value of s_0 and the integrals for I and S_b do not change during the electron's half bounce. As discussed in the following, the electrons complete a half bounce in just a few minutes compared to a period for the current sheet oscillation on the order of 10 h. Thus, our assumption for $\tau_b/2$ is valid. This same method was also applied by Regoli et al. (2016) to calculate half bounce times and azimuthal displacements of energetic ions near Titan's orbit in Saturn's magnetosphere.

Fig. 2(a) and (b) show the half bounce periods $\tau_b/2$ and azimuthal displacements r_{eq} (along the corotation direction) of several sample, *forward-traced* electrons with pitch angles of $\alpha_{eq} = 1°$ for a range of energies from 10^1 keV $\leq E \leq 10^4$ keV. Solid lines in Fig. 2(c) show the paths these electrons travel through Jupiter's magnetosphere. The electrons are initialized near Callisto when located at various distances h_{cs} to the center of Jupiter's magnetospheric current sheet, and equations (5)–(9) are solved to obtain $\tau_b/2$ and r_{eq}. Due to the negligibly small gyroradii of energetic electrons on magnetospheric scales, the paths in panel 2(c) correspond to the magnetic field lines along which the electrons travel.

Two different representations for Jupiter's magnetospheric field are considered in calculating $\tau_b/2$, r_{eq}, and the electrons' paths through the magnetosphere. The black lines in panels 2(a)–(c) use a purely dipolar field whose magnetic moment is centered at Jupiter and aligned with the planet's rotational axis (i.e., the 9.6° tilt between Jupiter's magnetic and rotational axes is not included). In such a field, Callisto is located within the magnetic equator of the dipole. In this model for Jupiter's magnetospheric field, the values of $\tau_b/2$ and r_{eq}, as well as the path traveled by electrons mirroring in Jupiter's northern hemisphere are identical to $\tau_b/2$, r_{eq}, and the path of an electron mirroring in the planet's southern hemisphere (for electrons with the same energy E and pitch angle α_{eq}).

The green, blue, and red lines in Fig. 2 represent electron motion using the superposition of the VIP4 model (Connerney et al., 1998) and the Khurana (1997) model for Jupiter's magnetospheric field. This representation of Jupiter's field considers the 9.6° tilt between Jupiter's magnetic and rotational axes. The VIP4 model describes the contributions of Jupiter's internal dynamo to the magnetospheric field, matching data from the Voyager and Pioneer spacecraft as well as observations of the location of Io's auroral footprint. The Khurana (1997) model uses an Euler potential representation of Jupiter's current sheet field, matching data from the two Voyager spacecraft. The green lines in panels 2(a)–(c) correspond to electron motion along a magnetospheric field line that threads Callisto when the moon is located at the center of Jupiter's current sheet ($h_{cs} = 0$ near $\lambda_{III} = 110°$ or $\lambda_{III} = 290°$). In this case, the bounce periods, azimuthal displacements, and paths traveled are identical for an electron mirroring at a northern or southern mirror point (for a given E and α_{eq}).

The red and blue lines in panels 2(a)–(c) show the energy dependence of $\tau_b/2$ and r_{eq}, as well as the paths traveled along a magnetospheric field line threading Callisto when the moon is located above the center of the Jovian current sheet (i.e., $h_{cs} > 0$). In this example, Callisto is located at a System III longitude of $\lambda_{III} = 260°$ and at 07:45 local time. The electron depicted by the blue path in Fig. 2(c) travels toward Jupiter's northern hemisphere, whereas the electron depicted by the path in red travels toward the south.

Fig. 2(a) shows that, for electrons initialized near Callisto's orbit with $\alpha_{eq} = 1°$, the half bounce times in a dipole (black) are nearly identical to the half bounce times near the center of Jupiter's current sheet (green)
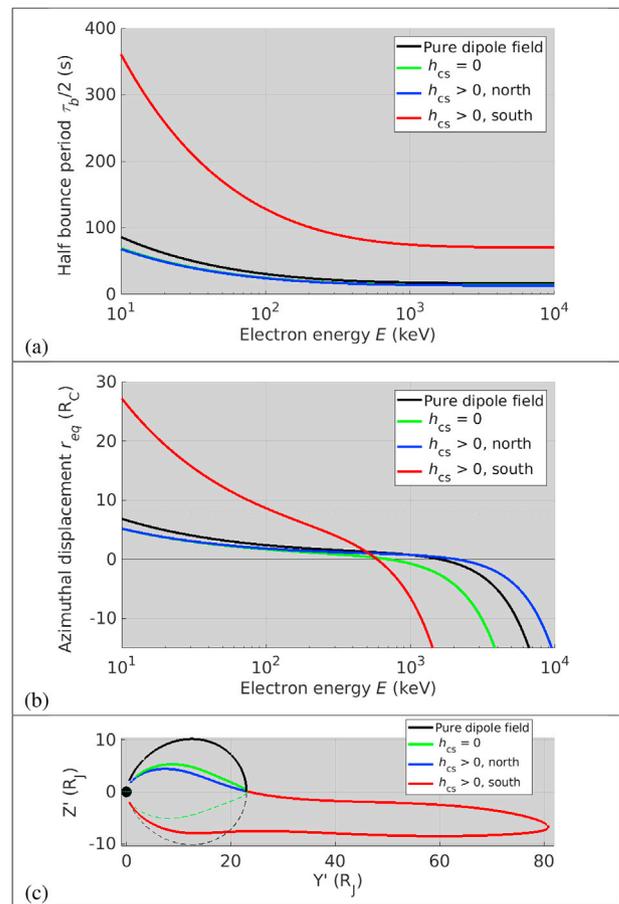
Fig. 2. Electron (a) half bounce periods $\tau_b/2$, (b) azimuthal displacements r_{eq} after a half bounce, and (c) paths through Jupiter's magnetosphere for a range of energies while traveling along three different magnetic field lines that thread Callisto at various h_{cs} values. For each representation of the magnetospheric field, the *forward-traced* electron is initialized near Callisto (i.e., in Jupiter's rotational equatorial plane at a radial distance of $26.3R_J$) with a pitch angle of $\alpha_{eq} = 1°$, travels to its mirror point, and then returns to the moon's local environment. The black line uses a spin-aligned dipole approximation for Jupiter's magnetic field, with Callisto located within the magnetic equatorial plane of the dipole. The green, blue, and red lines consider particle dynamics using the superposition of the VIP4 (Connerney et al., 1998) and Khurana (1997) models of Jupiter's magnetosphere. The green line corresponds to an electron launched at $h_{cs} = 0$ (i.e., within Jupiter's magnetic and rotational equators, a configuration that occurs only at the two crossings of Callisto with Jupiter's magnetic equator). The blue and red lines correspond to electrons initialized above the magnetic equator (i.e., for $h_{cs} > 0$) that travel either toward a northern mirror point (blue) or a southern mirror point (red). For such an electron, the path toward a mirror point in the northern hemisphere is much shorter than in the southern hemisphere (see blue/red field line segments in panel (c)). In this forward-tracing approach, positive values of r_{eq} in panel (b) denote an azimuthal displacement parallel to the corotation direction (i.e., toward downstream), whereas negative values denote a displacement antiparallel to corotation (toward upstream). Dashed lines in panel (c) correspond to the (symmetric) path an electron would travel if it were to mirror in the opposite hemisphere. The bounce paths in panel (c) are projected onto the Y'-Z' plane, in which the Y' axis is parallel to Jupiter's orbital motion and the Z' axis is aligned with Jupiter's rotation axis. Jupiter (black dot in panel (c)) is centered at $(Y', Z') = (0, 0)$. (For interpretation of the references to color in this figure legend, the reader is referred to the Web version of this article.)

for all energies shown. Although the black field line seems to be much longer, the green field line is bulged out of this plane due to sweepback of the Jovian field (Hill, 1979) and is longer than it appears. The half bounce times for the electrons traveling along these two field lines are also similar to $\tau_b/2$ for an electron mirroring in Jupiter's northern

hemisphere when Callisto is located at $h_{cs} > 0$ (depicted in blue in panel 2(a)). However, the bounce period of an electron that mirrors in Jupiter's southern hemisphere with Callisto located at $h_{cs} > 0$ (red) is more than *four times longer* than the other three bounce periods displayed. This is true for the entire energy range considered.

The reason for this disparity between the bounce periods displayed by the red and blue curves is revealed in panel 2(c). All four electrons start and end their half bounces near Callisto in the planet's rotational equatorial plane. However, differences in Callisto's *magnetic* latitude and thus, differing shapes of the bundle of field lines that thread the moon, cause the length of the path traveled by bouncing electrons through Jupiter's magnetosphere to vary drastically. Fig. 2(c) shows that an electron mirroring in Jupiter's southern hemisphere (red line) travels more than $80R_J$ away from Jupiter before the "guiding" magnetic field line turns back toward the giant planet. In our example with $h_{cs} > 0$, the point of minimum magnetic field intensity $|\mathbf{B}|$ along a field line threading Callisto is more than three times farther from Jupiter than the moon's orbital distance. This highly stretched structure of the fields lines near Callisto was also described by Paranicas et al. (2018), who have shown that, for $h_{cs} \neq 0$, Callisto may be connected to field lines with a minimum $|\mathbf{B}|$ occurring far beyond its orbital distance of $26.3R_J$ (and in this example, beyond $80R_J$). Hence, the path length of an electron initialized above Jupiter's magnetic equator ($h_{cs} > 0$) that mirrors in the planet's southern hemisphere is *substantially* longer than the path of an electron initialized above the magnetic equator but mirroring in the northern hemisphere (cf. red and blue segments in panel 2(c)).

Fig. 2(b) shows the azimuthal displacements r_{eq} of electrons after they mirror and return to Callisto's orbital plane. Only electrons below approximately 50 keV that are initialized *north* of Jupiter's current sheet ($h_{cs} > 0$) and mirror in Jupiter's *southern* hemisphere (red line) are displaced to values beyond $r_{eq} > 15R_C$ downstream of Callisto. Such electrons can not re-enter the region of perturbed fields generated by the moon's thermal plasma interaction, which Liuzzo et al. (2015) have shown to extend on the order of $10R_C$ along the corotation direction. However, electrons bouncing in the south with energies above approximately 50 keV (red curve) return to Callisto within $|r_{eq}| \ll 10R_C$. The same even holds true at lower energies (already occurring near 10 keV) for electrons in a dipole field (black), in the full magnetospheric field model with Callisto located at $h_{cs} = 0$ (green), and for electrons bouncing in Jupiter's northern hemisphere with Callisto above the current sheet ($h_{cs} > 0$, blue). Depending on the structure of the magnetospheric field near the moon, such electrons may have an additional opportunity to impact Callisto when returning to its orbit.

With increasing energy E, electrons reach a "critical" energy E_c, which occurs when the electron's magnetic drift velocity v_m cancels the relative velocity of the corotating plasma v_c (see, e.g., Khurana et al. (2008); Krupp et al. (2013)). In contrast to energetic ions where the magnetic drift velocity v_m is parallel to the corotation direction (along $+\hat{\mathbf{x}}$), the charge-dependence of v_m (see equation (6)) results in the magnetic drift for electrons being antiparallel to the corotation direction (along $-\hat{\mathbf{x}}$). Hence, near the critical energy E_c, an electron's azimuthal displacement after completing a half bounce is $r_{eq} \approx 0$. For the four cases displayed in panel 2(b), this occurs at energies as low as $E_c = 600$ keV (red line) and up to $E_c = 2,000$ keV (blue line).

Again, Fig. 2 displays values of electron half bounce period, azimuthal displacement, and path traveled through Jupiter's magnetosphere for Callisto located *above* the center of the current sheet ($h_{cs} > 0$). However, the physical effects illustrated by the blue and red lines are similar for Callisto located *below* the center of Jupiter's current sheet ($h_{cs} < 0$) as well, and also similar for other electron pitch angles $\alpha_{eq} \neq 1°$. We also note that the opening angle of the loss cone for energetic electrons near Callisto's orbit is way below $1°$, so nearly no energetic electrons are lost to Jupiter's atmosphere before mirroring. This is clearly visible in Fig. 2(c), as electrons launched near Callisto with $\alpha_{eq} = 1°$ still mirror well above the planet.

2.3.2. Combining the local and global models

Overall, Fig. 2 reveals that, in contrast to energetic ions, the bounce motion of energetic electrons can *not* be ignored when studying their dynamics near Callisto, since their azimuthal displacement after bouncing may be $|r_{eq}| \ll 10R_C$ or even $|r_{eq}| < 1R_C$. Hence, treating the electromagnetic fields as constant outside of the hybrid simulation domain and discontinuing the *back-tracing* of energetic particles after multiple local gyrations (as done by Liuzzo et al. (2019) for ions) is *not* appropriate for electrons. Even approximating Jupiter's magnetospheric field as dipolar near Callisto's orbit leads to incorrect estimations of the electron's half bounce period $\tau_b / 2$ and its azimuthal displacement.

Therefore, our study uses the magnetic field obtained from the combined VIP4 (Connerney et al., 1998) and Khurana (1997) models to calculate the azimuthal displacements r_{eq} of energetic electrons once they leave the AIKEF domain. If an energetic electron reaches the $\pm y$ or $\pm z$ face of the hybrid simulation domain, GENTOo calculates the electron's displacement r_{eq} in the x-direction as it bounces in the ambient magnetospheric field based on the particle's energy and pitch angle (see equations (5)–(9)) when it leaves the box. GENTOo does *not* solve the Newtonian equation of motion (equation (1)) for electrons outside of the AIKEF simulation domain. This approach is applied because the computational resources required to calculate the trajectories of 6.7 million energetic electrons as they travel throughout Jupiter's entire magnetosphere are too vast for even a single GENTOo simulation.

After completing a half bounce, the electron is re-injected at the same $\pm y$ or $\pm z$ face of the AIKEF box from which it exited and with its velocity component parallel to the magnetic field reversed. In our back-tracing model, the x-position at which the electron is re-injected is offset by its *negative* azimuthal displacement r_{eq}: an electron for which equations (5)–(9) yield an azimuthal displacement $r_{eq} > 0$ is displaced toward upstream in the *back-tracing* approach, whereas an electron with $r_{eq} < 0$ is displaced toward downstream in the *back-tracing* approach. For back-traced electrons in the electromagnetic field configurations used for this study (see Sections 3 and 4), their discrete initial energies E are chosen such that they are sufficiently far from their critical energy E_c. Otherwise, electrons may bounce indefinitely without any discernible azimuthal displacement which can not be modeled by GENTOo.

After re-injection, the electron again travels through Callisto's perturbed electromagnetic environment and is traced through the fields from the hybrid simulation. This sequence (tracing, re-injection, tracing, etc.) repeats until either the electron's position becomes $|\mathbf{r}| < 1.05R_C$ and it is "forbidden" (i.e., the electron can *not* contribute to energetic electron precipitation) or the azimuthal position of the electron is $|x| > 15R_C$ (i.e., after exiting the upstream or downstream face of the AIKEF simulation domain). In this latter case, the electron is finally considered "allowed." Such an electron *can* precipitate onto Callisto in a forward-tracing approach: any subsequent bounces would cause the electron to return even farther from Callisto and it could not re-encounter the moon's locally perturbed electromagnetic environment.

During an electron's bounce motion, the position of the guiding field line changes with respect to the moon. An electron that leaves Callisto's environment along a field line that threads, for example, the ramside pileup region may impinge onto the moon's *wakeside* atmosphere after bouncing, since the field line may have been stretched farther downstream (due to convection) during the half bounce period. Although the field lines in the stationary AIKEF output do not change in time (i.e., any given field line neither moves nor changes its shape), these effects are taken into account by our model. An electron that leaves the AIKEF domain along a certain guiding field line is re-injected along a different field line after bouncing, displaced against the original one by r_{eq}.

At Titan, Snowden et al. (2013) and Snowden and Yelle (2014) have highlighted the importance of including such effects to understand energetic electron precipitation onto the moon's atmosphere. The short bounce times of energetic electrons in Saturn's magnetic field (compared to the time scales of magnetospheric convection) and the locations where

they re-enter Titan's perturbed plasma environment are associated with significant inhomogeneities in the energy deposition rates into Titan's upper atmosphere by precipitating electrons.

At the upper end of the energy range considered for this study (above $E \approx 10^4$ keV), the azimuthal displacement of bouncing electrons is $|r_{eq}| \gg 15R_C$ after mirroring (see Fig. 2(b)). Thus, once such an electron bounces, it can not re-enter Callisto's local environment and it has an "allowed" trajectory. At energies $E < 10^4$ keV, Fig. 2(b) shows that the azimuthal displacement $|r_{eq}|$ of mirroring electrons is on the order of $1 - 10R_C$. The gyroradii of electrons at these energies are still below $0.5R_C$ (see Table 2), and in the region of enhanced magnetic field near Callisto, they are further reduced to values below $r_g \approx 0.25R_C$. Hence, electrons at energies $E < 10^4$ keV are unable to gyrate around Callisto to evade impacting the starting grid. Therefore, the *gyrophase* of a re-injected electron after bouncing (i.e., its velocity vector perpendicular to the magnetic field) has no relevance on whether or not its trajectory is forbidden and is left unchanged during re-injection at a face of the AIKEF box. If the tube-like envelope around an electron's helical trajectory intersects the starting grid, its trajectory will *always* be forbidden. The location *where* a back-traced electron impacts the starting grid has no influence at all on the resulting precipitation patterns—indeed, such a forbidden electron has no counterpart in a forward-tracing approach. All that matters is *that* the electron hits the grid and its trajectory is forbidden.

In summary, unlike for energetic *ions* (see Liuzzo et al. (2019)), the azimuthal displacements r_{eq} of energetic *electrons* after a half bounce $\tau_b / 2$ must be considered when investigating their precipitation onto Callisto. In order to determine electron displacements along the corotation direction after bouncing, we couple output from the AIKEF model of Callisto's local interaction region (Liuzzo et al., 2015, 2016) with displacements r_{eq} obtained from a global analytical model of Jupiter's magnetospheric environment (Roederer, 1967; Connerney et al., 1998; Khurana, 1997). A schematic of the model setup is shown in Fig. 3. Once electrons leave the hybrid simulation domain (represented by the green box), values of $\tau_b / 2$ and r_{eq} are calculated via equations (5)–(9). After they mirror and return to the moon's local environment, electrons are

re-injected at an azimuthal displacement r_{eq} (blue in Fig. 3) into the hybrid simulation domain and GENTOo again calculates their trajectory through the draped fields within the box. Our approach thereby allows for the possibility of returning energetic electrons to travel through Callisto's perturbed electromagnetic environment multiple times before determining their fate (i.e., an "allowed" or "forbidden" trajectory) in the back-tracing approach.

3. Accessibility of Callisto to energetic electrons

To quantitatively compare the spatial distribution of Callisto's accessibility to energetic electrons for different thermal plasma interaction scenarios and different initial electron kinetic energies, we define an energy-dependent accessibility $\lambda(\tilde{\mathbf{r}}_C, E)$ for each point on the starting grid (analogous to Regoli et al. (2016) and Liuzzo et al. (2019)):

$$\lambda(\tilde{\mathbf{r}}_C, E) = \frac{N_a(\tilde{\mathbf{r}}_C)}{N_p} \quad . \tag{10}$$

Here, $\tilde{\mathbf{r}}_C$ represents a given point on the spherical starting grid of radius $|\tilde{\mathbf{r}}_C| = \tilde{R}_C$. The quantity N_p is the total number of electrons launched from *each point* on the grid (i.e., $N_p \approx 2,600$ electrons), and $N_a(\tilde{\mathbf{r}}_C)$ is the number of electrons launched at that specific point with "allowed" trajectories. This parameter ranges from $\lambda = 0\%$ for a location where no electrons have allowed trajectories, to $\lambda = 100\%$ at a location where every electron has an allowed trajectory and can precipitate onto the moon's atmosphere.

3.1. Energetic electron accessibility: very weak plasma interaction (Run #1)

Maps displaying the accessibility λ of Callisto to energetic electrons are shown in Fig. 4 for select energies and for the electromagnetic fields of Run #1. These fields correspond to Callisto located at $h_{cs} \gg 0$, where a weak interaction of the moon's induced magnetic field with the Jovian thermal magnetospheric plasma occurs (see Table 1). The interaction between Callisto's ionosphere and the magnetospheric plasma is *not*
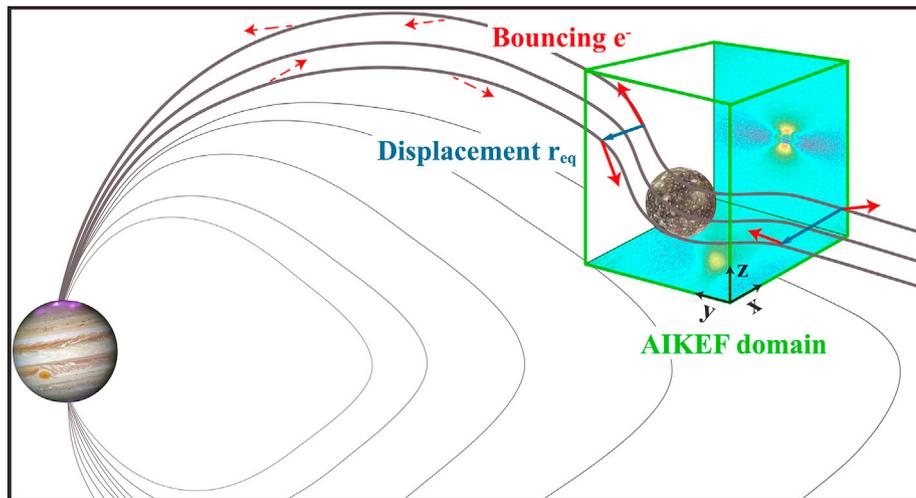

Fig. 3. Schematic displaying the coupling between the local AIKEF model of Callisto's perturbed electromagnetic environment and a global representation of Jupiter's magnetospheric field. The AIKEF simulation domain is displayed in green, and the modeled bulk velocity of the locally deflected thermal plasma flow near the moon is shown at two faces of the box. The x, y, and z axes of the local CphiO coordinate system are also included. Magnetospheric field lines, locally draped around Callisto, are shown in black. The red arrows along the field lines denote the momentary velocity vectors of a few select electrons as they (solid red) enter and leave the AIKEF domain or (dashed red) bounce through the magnetosphere. As soon as energetic electrons leave the domain of the hybrid simulation, GENTOo calculates their half bounce times $\tau_b / 2$ and azimuthal displacements r_{eq} using the method presented in Roederer (1967) for Jupiter's magnetospheric field (Connerney et al., 1998; Khurana, 1997). After mirroring, the electrons return to the AIKEF box, are re-injected into the simulation domain, and again travel through Callisto's perturbed electromagnetic environment. For a given energetic electron in GENTOo, this process may repeat multiple times. The figure is not to scale. Jupiter/Callisto image credit: Smithsonian Astrophysical Observatory Chandra X-ray Center/NASA. (For interpretation of the references to color in this figure legend, the reader is referred to the Web version of this article.)
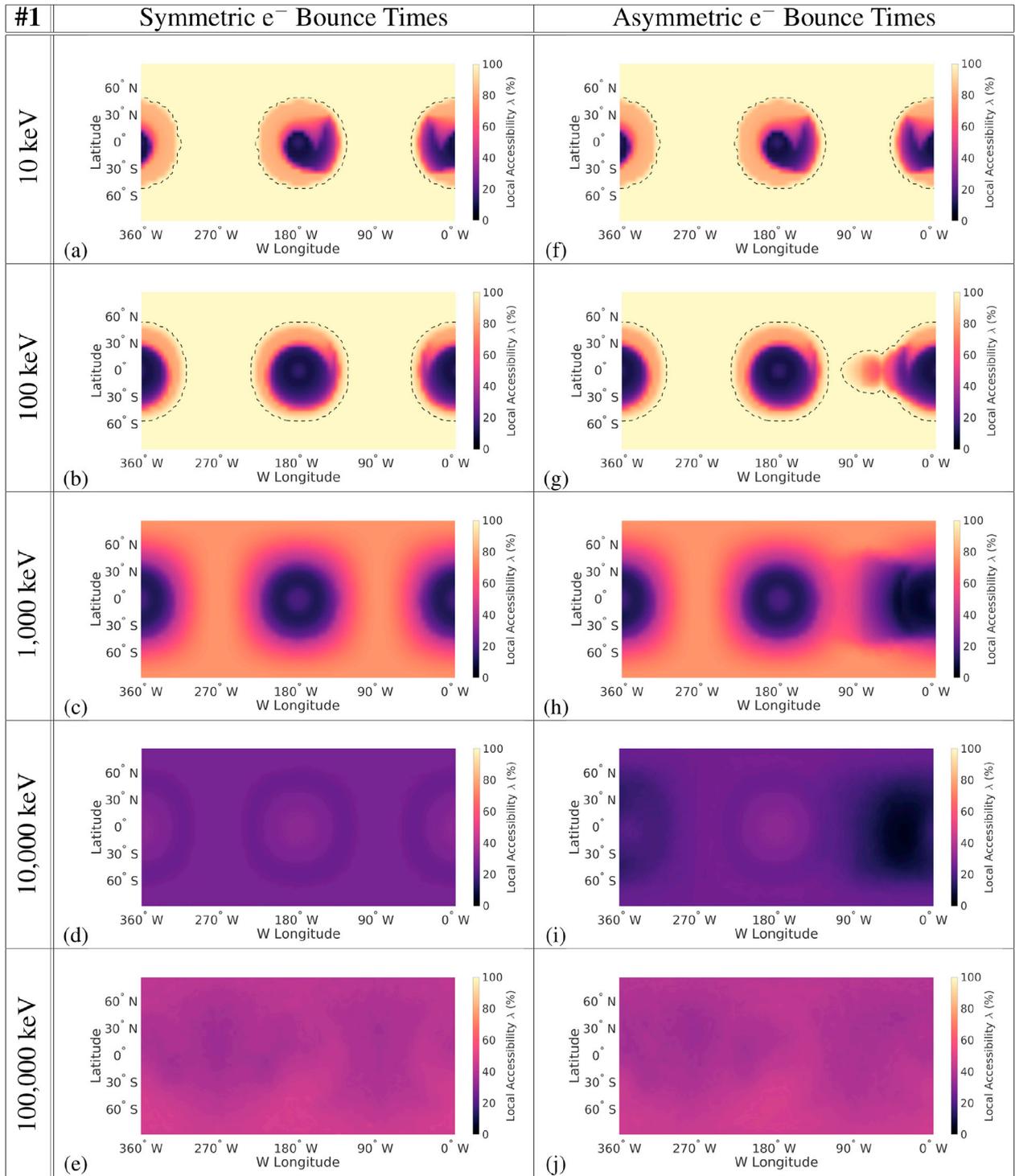
Fig. 4. Energetic electron accessibility λ of Callisto at select energies for the electromagnetic fields of Run #1, corresponding to a weak interaction with Callisto's induced dipole alone (see Table 1). Lowest accessibility values are depicted in black, whereas highest values are in yellow. Dashed lines in panels (a), (b), (f), and (g) denote the inner boundaries of regions with $\lambda \geq 99\%$ accessibility. The "symmetric" (panels (a)–(e)) or "asymmetric" (panels (f)–(j)) distinction denotes the method used to calculate the mirroring electrons' bounce times and azimuthal displacements; see text for further details. A description of the latitude and longitude convention used can be found in the text. (For interpretation of the references to color in this figure legend, the reader is referred to the Web version of this article.)

included in this scenario. In each panel of Fig. 4, the horizontal axis displays West Longitude on the starting grid from which energetic electrons are launched, increasing from right to left. In this convention, 0° W longitude is located in Callisto's Jupiter-facing hemisphere, aligned with the $+y$-axis of the CphiO system (located at $x = 0, y = +1\tilde{R}_C$ in Callisto's equatorial plane). Moving clockwise, 90° W is located in Callisto's orbital leading hemisphere; in Callisto's equatorial plane, this longitude is co-

located with the apex of the moon's orbital leading hemisphere (i.e., at $x = +1\tilde{R}_C, y = 0$). The 180° W line of longitude is antipodal to 0° W, and located in Callisto's Jupiter-averted hemisphere (at $x = 0, y = -1\tilde{R}_C$ in the equatorial plane), whereas 270° W is located in the moon's trailing (ramside) hemisphere. The vertical axis in each panel of Fig. 4 displays latitude, with 90° N located at Callisto's geographic north pole and 90° S at the south pole.

Fig. 4(a)–4(e) display maps of λ using the *same* values of the half bounce periods $\tau_b/2$ and azimuthal displacements r_{eq} for electrons bouncing in Jupiter's northern and southern hemispheres. For each combination of electron energy and equatorial pitch angle, the $\tau_b/2$ and r_{eq} used are an average between these values in the planet's two hemispheres. Using the elongated electron path displayed in Fig. 2(c) as an example, this average would be taken between the (blue) northern and (red) southern segments of the field line.

In the *back-tracing* approach, an electron of a given energy that leaves the AIKEF domain with a velocity component parallel to the magnetic field bounces in Jupiter's *northern* hemisphere. In the model setup for panels 4(a)–4(e), such an electron is displaced azimuthally by an identical distance r_{eq} as an electron that leaves the hybrid box with a velocity antiparallel to $\mathbf{B}_0$ and bounces in Jupiter's *southern* hemisphere. Hence, the values of $\tau_b/2$ and r_{eq} for these two electrons are "symmetric" (see the left column of Fig. 4). When Callisto is located at $h_{cs} \gg 0$ or $h_{cs} \ll 0$, the values of $\tau_b/2$ and r_{eq} are drastically different for electrons mirroring in Jupiter's northern and southern hemispheres (see Fig. 2). However, in order to investigate the effect that this asymmetric bouncing may have on accessibility patterns, we first focus on the case with "symmetric" values, and will subsequently identify differences to the patterns obtained with "asymmetric" bouncing (panels 4(f)–4(j)).

For electrons with energies $E \leq 100$ keV, panels 4(a) and 4(b) show that the accessibility is nearly $\lambda \approx 100\%$ everywhere except for two circular regions centered at Callisto's equator near 0° W and 180° W longitude. Within these two areas which individually cover approximately 20% of the starting grid's surface, the electron accessibility rapidly drops to values below 10%. These circular segments of reduced accessibility coincide with the regions above the "magnetic poles" of Callisto's induced dipole. Since Callisto's induced magnetic moment is antiparallel to the magnetospheric background field, the total magnetic field on Callisto's surface at the "magnetic poles" is $|\mathbf{B}| = 0$ (Zimmer et al., 2000). Slightly above the surface (i.e., at $\tilde{r}_C$), but still near the "poles," the field is reduced to $|\mathbf{B}| \ll |\mathbf{B}_0|$. Thus, the magnitude of the total field $|\mathbf{B}|$ increases with distance to the moon's "magnetic poles," approaching $|\mathbf{B}_0|$ at large distances (see Figs. 1(e) and 5).

The mechanism causing these two circular regions of reduced accessibility is revealed in Fig. 5, which shows the trajectories of two sample energetic electrons (white lines) superimposed onto color contours that display the magnetic field magnitude of Run #1 in Callisto's equatorial ($z = 0$) plane. Arrows denote the *back-traced* electrons' directions of travel and magnetic field lines are included in black. The electrons are initialized within Callisto's equatorial plane at 45° W longitude, with initial velocity vectors in this plane that are offset from local zenith by ±30°. As the *back-traced* electrons travel farther from the moon, the contribution of Callisto's induced dipole to the local magnetic field decreases with a r^{-3} dependence. As a result, these electrons experience an *increasing* magnetic field magnitude as they travel along the field lines away from the moon. However, before the electrons can escape Callisto's local environment, the enhanced magnetic field causes them to mirror within approximately $2R_C$ of the moon. After mirroring, the *back-traced* electrons turn back toward Callisto, impact the starting grid, and become forbidden.

Hence, in the *back-tracing* approach, the local field configuration near Callisto's magnetic poles acts as a "magnetic bottle" with Callisto filling its center. This effect reduces the accessibility λ of energetic electrons near both poles. Close to the magnetic poles, *back-traced* electrons are initialized within a region of $|\mathbf{B}| \ll |\mathbf{B}_0|$, but are confined close to the moon's surface as they move along the magnetic field lines and experience an enhanced field, mirror, and subsequently re-encounter the starting grid. In a *forward-tracing* approach, electrons from outside the moon's local environment would travel along the magnetic field lines toward Callisto. These electrons are then guided by the locally curved magnetic field lines near Callisto (see Fig. 5) and are diverted around the moon's magnetic poles, unable to precipitate in these regions. Thus,
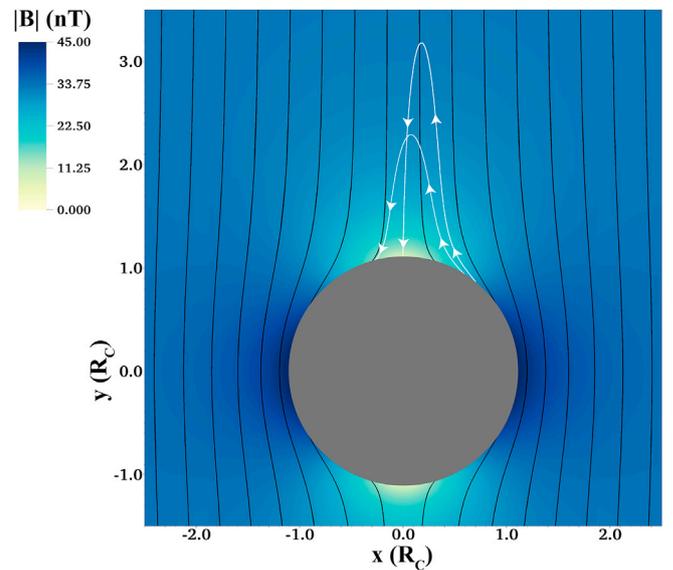

Fig. 5. Trajectories of two forbidden energetic electrons in the electromagnetic fields of Run #1. The electrons' paths are displayed in white, with arrows denoting their direction of travel in the *back-tracing* approach, projected onto the *x-y* plane of the CphiO system. Colored contours of the magnetic field magnitude are included with field lines displayed in black. These two electrons are initialized near the Jupiter-facing "pole" of Callisto's induced field, within the geographic equatorial ($x–y$) plane at 45° W longitude; i.e., at a position $[x,y, z] = [\tilde{R}_C\cos(45°), \tilde{R}_C\sin(45°), 0]$. Their initial velocity vectors are located in this plane and are offset from zenith by ±30°. Callisto and the electron starting grid of radius $\tilde{R}_C$ are represented by the gray circle.

without currents generated by Callisto's plasma interaction (i.e., for the electromagnetic fields of Run #1), the induced dipole alone carves a depletion in the accessibility pattern of energetic electrons near the magnetic poles.

However, with increasing azimuthal distance from the magnetic poles, Callisto's induced field become more aligned with the direction of the magnetospheric background field.; i.e., the contribution of induction *enhances* the total magnetic field strength. Thus, away from the magnetic poles, *back-traced* energetic electrons are initialized within a region of magnetic field $|\mathbf{B}| \geq |\mathbf{B}_0|$ (see Fig. 5), with the maximum magnitude $|\mathbf{B}| = 2|\mathbf{B}_0|$ reached at Callisto's "magnetic equator" (at $x^2 + z^2 = R_C^2$ and $y = 0$, see Kivelson et al. (1999)). After initialization, such *back-traced* electrons quickly enter regions where the total field is reduced compared to $|\mathbf{B}|$ at their starting point. Thus, these electrons do *not* mirror close to Callisto within the locally perturbed magnetic field, but rather travel along the field lines until they exit the AIKEF box. At energies $E \leq 100$ keV, *back-traced* electrons are displaced far enough toward upstream after bouncing (see Fig. 2(b)) that they will not return to Callisto and eventually escape with allowed trajectories. Thus, away from the magnetic poles of Callisto's induced field, the accessibilities in panels 4(a) and 4(b) reach values of $\lambda = 100\%$.

For $E = 10^3$ keV (see panel 4(c)), the maximum accessibility value at any point on the starting grid remains well below $\lambda = 100\%$. However, the overall accessibility pattern is still qualitatively similar to the patterns at lower energies. In particular, the two circular regions of reduced accessibility, centered at 0° W and 180° W longitude, are still clearly discernible. This sudden, "switch-like" global decrease in the value of λ occurs as soon as the gyroradius of the energetic electrons becomes $r_g > 0.05R_C$ (i.e., it exceeds the radial distance between the starting grid and the hard cutoff for forbidden electrons). At and above this energy of $E = 10^3$ keV, *back-traced* electrons may immediately gyrate into this cutoff located at an altitude of $1.05R_C$. At lower energies, electron gyroradii are so small that they are able to complete a full gyration inside of the narrow gap between the starting grid and the lower boundary without impacting.

The specific energy at which this "switch" in the accessibilities occurs is dependent on the location of this cutoff: for cutoff altitudes above $1.05R_C$ this would occur at slightly smaller energies than $E = 10^3$ keV, whereas for cutoff altitudes below $1.05R_C$ it would occur at slightly larger energies. Hence, this "switch" in the accessibility value is related to the model setup. If the gap between the starting grid and the cutoff were zero, the maximum possible accessibility value would be $\lambda = 50\%$ at *every* location and energy. In this case, half of the initialized electrons would immediately impact the starting grid and they would not survive a single time step in GENTOo. However, the structures visible in Fig. 4 would still be qualitatively the same, with a strong decrease in λ located near the magnetic poles of Callisto's induced field.

At $E = 10^4$ keV (see Fig. 4(d)), the two distinct circular depletions visible at lower energies have nearly disappeared; only two narrow "rings" of reduced λ are faintly visible around Callisto's magnetic poles. Compared to panel 4(c), the overall accessibility is further reduced. For an energy of $E = 10^5$ keV displayed in panel 4(e), the accessibility pattern is nearly uniform. At this highest energy considered, electron gyroradii clearly exceed the radius of Callisto (see Table 2); i.e., the relative size of the Callisto obstacle shrinks to the *back-traced* electrons and they are able to gyrate around the moon without ever re-encountering the starting grid. Hence, the accessibility pattern approaches a global value of $\lambda = 50\%$, similar to the accessibility of Callisto to high-energy magnetospheric ions (Liuzzo et al., 2019).

To understand the effect that different half bounce times for electrons mirroring in Jupiter's northern and southern hemispheres have on the accessibility patterns, the right column of Fig. 4 includes additional maps of λ at the same energies as panels 4(a)–4(e). However, for the right column, the electrons' azimuthal displacements r_{eq} after bouncing are calculated using "asymmetric" values of $\tau_b/2$ and the maps of λ are displayed in panels 4(f)–4(j). For this case of "asymmetric" bouncing, the half bounce time and path traveled by an electron that mirrors in Jupiter's northern hemisphere are much shorter than for an electron mirroring in Jupiter's southern hemisphere (for $h_{cs} > 0$, as used in Run #1, and for a given E and α_{eq}). Using Fig. 2(c) as an example, the bounce path of an electron mirroring in Jupiter's northern hemisphere is displayed by the blue segment, and the path of an electron mirroring in the southern hemisphere corresponds to the red segment.

At the lowest and highest energies considered in this study (i.e., $E = 10$ keV in panel 4(f) and $E = 10^5$ keV in panel 4(j)) the accessibility patterns are indistinguishable between the "symmetric" and "asymmetric" cases (cf. Fig. 4(a) and (e)). However, for electrons at the three energies in between (10^2 keV, 10^3 keV, and 10^4 keV), an additional region of reduced accessibility to $\lambda \approx 70\%$ forms in Callisto's Jupiter-facing, downstream hemisphere between 0° W and 90° W longitude (i.e., $> 0, y > 0$). This feature does *not* have a counterpart in the Jupiter-

averted hemisphere. This effect is further illustrated in Fig. 6, which displays the accessibility maps of 10^3 keV electrons for the cases of (panel (a)) "symmetric" and (panel (b)) "asymmetric" bouncing. These profiles are identical to the ones in Fig. 4(c) and (h), but are now displayed on a sphere of radius $\tilde{R}_C$. The look direction in both panels of Fig. 6 is from a point located downstream of Callisto that is offset slightly northward, with Jupiter toward the right of the panels.

For the electromagnetic field configuration of Run #1, electrons that exit the AIKEF domain in Callisto's Jupiter-*facing* hemisphere bounce in Jupiter's *northern* hemisphere, whereas electrons that exit in the Jupiter-*averted* hemisphere bounce in Jupiter's *southern* hemisphere. Due to their vastly shorter bounce paths through Jupiter's magnetosphere, electrons that bounce in the north return much closer to Callisto after mirroring compared to electrons bouncing in the south (because $h_{cs} > 0$, see Fig. 2(c)). Electrons that mirror in Jupiter's northern hemisphere also return at a smaller azimuthal displacement r_{eq} than in the case of "symmetric" bouncing (see Fig. 2).

For electrons initialized near 30° W longitude, it is "easier" to leave the AIKEF domain at the $+y$ face of the simulation domain and bounce in Jupiter's northern hemisphere than it is to leave at the $-y$ face and bounce in the south. In order for such an electron to bounce in Jupiter's southern hemisphere, it would need to first circumvent Callisto. The opposite holds true for electrons initialized near 150° W longitude: in order to exit at the $+y$ face of the AIKEF domain, these electrons would first need to travel around Callisto and avoid impacting the starting grid in the process.

Due to the smaller r_{eq} for electrons bouncing in the north, more electrons initialized near 30° W longitude impact the starting grid and become forbidden after mirroring, generating an additional depletion in the accessibility map (see Fig. 6(b)). For instance, when a *back-traced* electron initialized near 30° W longitude with an energy of 10^3 keV and equatorial pitch angle $\alpha_{eq} = 1°$ mirrors in Jupiter's northern hemisphere, it is displaced $1R_C$ after bouncing (see Fig. 2(b)). Hence, this electron is not displaced far enough from Callisto to avoid re-encountering the locally perturbed fields. Such an electron therefore has a high likelihood of becoming forbidden on its subsequent journey through Callisto's perturbed electromagnetic environment. However, a *back-traced* electron of the same energy initialized near 150° W that mirrors in the south (i.e., with $\alpha_{eq} = 179°$) experiences a displacement of $6R_C$ and would never impact the grid. When Callisto is located *below* the center of Jupiter's magnetospheric current sheet (with $h_{cs} < 0$; i.e., the alternate scenario to the case shown here for $h_{cs} > 0$), the opposite is true: more electrons initialized in Callisto's Jupiter-averted hemisphere near 150° W would be forbidden, and the additional region of reduced accessibility would be mirrored against the 90° W meridian.

Overall, our results for the electromagnetic fields of Run #1 show that
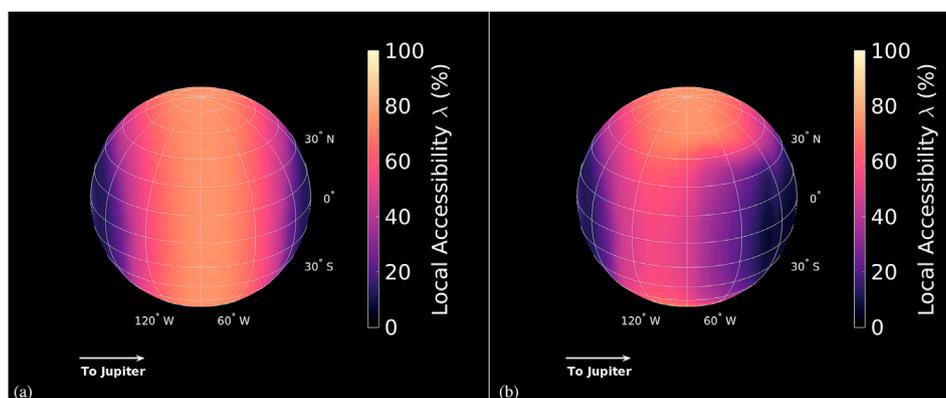

Fig. 6. Accessibility of 10^3 keV electrons for the (a) symmetric and (b) asymmetric models of $\tau_b/2$ and r_{eq} (see text and Fig. 4 for further details). The look direction is from a point in Callisto's downstream hemisphere (at 90° W longitude) that is displaced slightly northward, with Jupiter located to the right. The values of λ are projected onto a sphere of radius $\tilde{R}_C$.

at larger energies, electron gyration becomes increasingly important in shaping the electron precipitation patterns onto Callisto. Hence, a guiding center approach would *not* be applicable in generating such maps. In addition, although the differences in the half bounce times and azimuthal displacements between Jupiter's northern and southern hemispheres are drastic (see Fig. 2 and discussion in Section 2.3), there are only subtle changes in the accessibility patterns of energetic electrons between the cases of symmetric and asymmetric bouncing. Therefore, accessibility maps for the case of asymmetric bouncing will *not* be shown in subsequent sections.
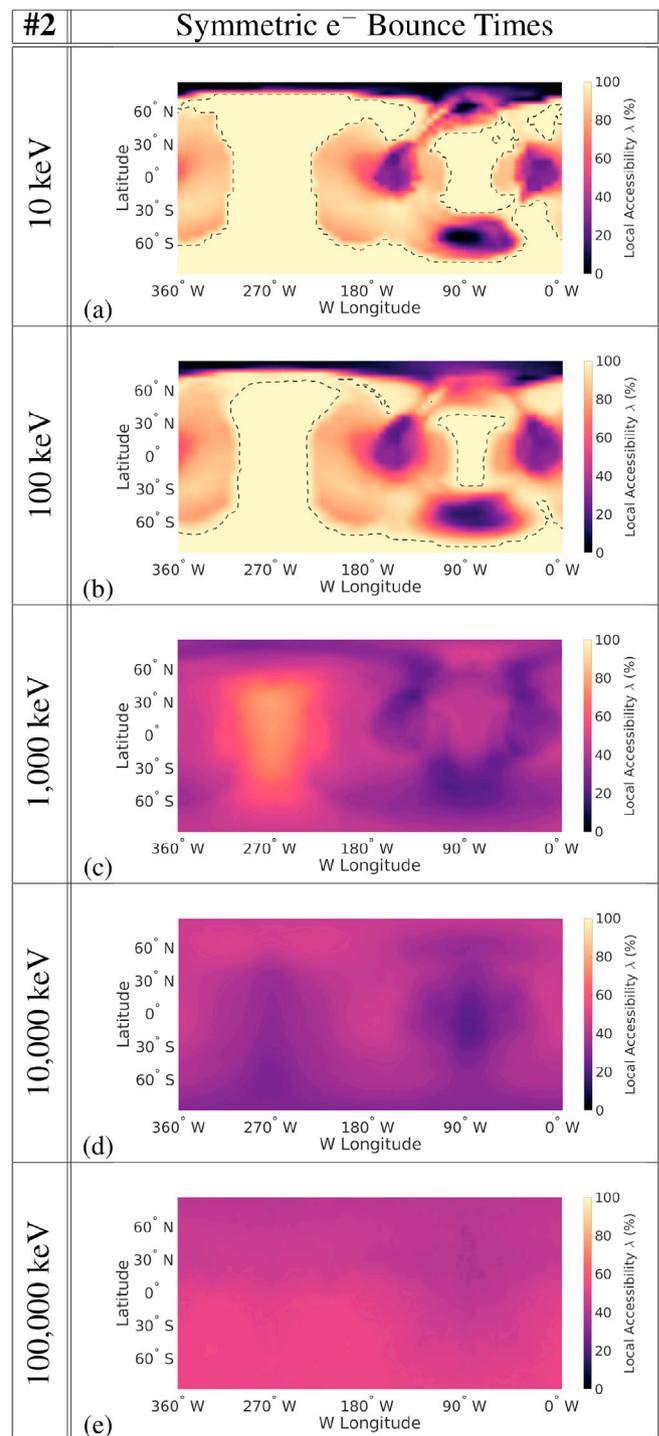
3.2. Energetic electron accessibility: stronger plasma interaction with Callisto's induced dipole (Run #2)

The accessibility of Callisto to energetic electrons for the electromagnetic fields of Run #2 is shown in Fig. 7. These fields correspond to a stronger interaction (compared to Run #1) with Callisto's induced dipole alone, again without the presence of Callisto's ionosphere, as observed by Galileo's magnetometer during the Galileo C3 and C9 flybys (Liuzzo et al., 2015). In Run #2, plasma interaction currents are no longer neglected.

Panels 7(a) and 7(b) display the accessibility maps of 10 keV and 100 keV electrons, respectively. At these energies, Callisto's orbital trailing (ramside) hemisphere near 270° W longitude displays values of $\lambda \approx 100\%$. This "stripe" of high accessibility in the trailing hemisphere starts at the moon's south pole, but extends only to northern latitudes of about 75° N (see dashed lines in panels 7(a) and 7(b)). Near the "magnetic poles" of Callisto's induced dipole (located in the equatorial plane at 0° W and 180° W longitude), electron accessibility is again reduced, here to values below $\lambda \approx 30\%$. Similar to Run #1, the field configuration near Callisto's magnetic poles acts as a "magnetic bottle," causing *backtraced* electrons to re-encounter the starting grid soon after initialization (see Fig. 5). However, the transition from regions of high to low λ are more gradual and the pattern is more blurred in Run #2 compared to Run #1.

A major difference in the accessibility maps between Runs #1 and #2 (for electrons with $E \leq 100$ keV) is a pronounced north/south asymmetry that occurs when plasma currents are considered (Run #2, see panels 7(a) and 7(b)). In contrast to Callisto's south polar cap where $\lambda = 100\%$ everywhere, the entire north polar cap is devoid of electron precipitation at latitudes poleward of 75° N. The reason for this asymmetry becomes evident in Fig. 8, which depicts a three-dimensional visualization of λ for 10 keV electrons (panel 8(a)) as well as the electric field near the moon obtained from the AIKEF model (panel 8(b)). In Run #2, the undisturbed convective electric field $\mathbf{E}_0 = -\mathbf{u}_0 \times \mathbf{B}_0$ is aligned with the $+z$-axis. With a bulk velocity of $|\mathbf{u}_0| = 192$ km/s, the gyroradii of the *thermal* magnetospheric O^+ ions near Callisto are approximately $r_g \approx 0.5 R_C$, so gyration of the upstream ions is non-negligible compared to the size of the moon. Hence, the deflection of the plasma around Callisto, as well as the resulting electromagnetic field perturbations, are (slightly) asymmetric between the moon's northern and southern hemispheres.

Magnetospheric plasma slowdown in Callisto's ramside hemisphere generates a magnetic field enhancement, whereas downstream, $|\mathbf{B}|$ is reduced as the wakeside magnetic cavity begins to form (see Fig. 1). As can be seen in Fig. 2 of Liuzzo et al. (2019), this region of reduced $|\mathbf{B}|$ also extends above Callisto's geographic north pole. These magnetic structures manifest in the electric field as regions with an enhanced $|\mathbf{E}|$ upstream of the moon and a reduced electric field downstream. However, Fig. 8(b) shows that the electric field perturbations are slightly asymmetric between Callisto's northern and southern hemispheres (due to the non-negligible ion gyration): the regions of enhanced/reduced $|\mathbf{E}|$ are rotated around the moon in a counter-clockwise direction. The extensions of the regions with enhanced/reduced electric field magnitude are also slightly different between the northern and southern hemispheres. In Callisto's southern hemisphere, the region of *enhanced* $|\mathbf{E}|$ (red) surrounds the entire polar cap, and the electric field void (blue) is rotated

Fig. 7. Energetic electron accessibility at select energies for the electromagnetic fields of Run #2, a stronger plasma interaction with Callisto's induced dipole alone (see Table 1). The energies displayed are the same as in Fig. 4. The accessibilities are calculated for electron bounce times and azimuthal displacements that are "symmetric" between Jupiter's northern and southern hemispheres. Dashed lines in panels (a) and (b) correspond to the inner boundaries of regions where $\lambda \geq 99\%$. See Fig. 4 and the text for further description.

into the moon's wake. In the northern hemisphere, the region of *reduced* $|\mathbf{E}|$ surrounds only part of the moon's polar cap. If pickup of ionospheric particles (with even larger r_g than the thermal upstream ions) were taken into account, these asymmetries would be even more pronounced (cf. Figs. 5 and 6 in Liuzzo et al. (2015) as well as Figs. 2 and 3 in Liuzzo et al.
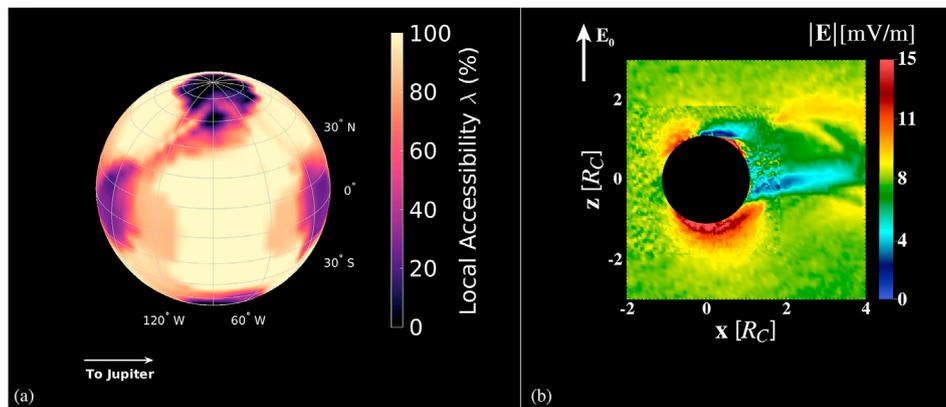
Fig. 8. (a) Accessibility of 10 keV electrons for the electromagnetic fields of Run #2. The look direction is the same as in Fig. 6. (b) Electric field magnitude |**E**| near Callisto for Run #2 in the x-z plane. The background electric field **E₀** points northward. Callisto and the starting grid for energetic electrons are represented by the black circle.

(2019)).

Although the electric field decrease visible in Callisto's northern hemisphere is small compared to length scales of the moon's thermal plasma interaction, it has a tremendous influence on the dynamics of energetic electrons which occur on much smaller scales. Within the localized electric field void above Callisto's north pole (blue in Fig. 8(b)), the contribution of the $\mathbf{E} \times \mathbf{B}$ drift to the motion of newly-injected, *back-traced* electrons is negligible. For energies $E \leq 100$ keV, the gyroradii of electrons ($r_g \approx 10^{-2}R_C$, see Table 2) are much smaller than the size of this void which extends approximately $0.5R_C$ northward (see Fig. 8(b)). Hence, electrons injected "below" this void are unable to pass through this region, neither by $\mathbf{E} \times \mathbf{B}$ drift nor by gyration. Instead, they remain near Callisto, ultimately re-encounter the starting grid, and become forbidden. This causes a region of $\lambda \approx 0$ that covers Callisto's north polar cap (see Fig. 8(a)). Similarly, the stretched electric field void in Callisto's southern hemisphere (see panel 8(b)) results in an additional oval λ depletion best visible in panels 7(a) and 7(b) between 35° S and 60° S.

In a *forward-tracing* picture, electrons with energies $E \leq 100$ keV would approach Callisto and become "captured" within these localized electric field depletions near the moon. Their $\mathbf{E} \times \mathbf{B}$ drift velocity would become negligible and they would not be able to approach Callisto any further (at least not on time scales of a few hours during which the assumption of constant magnetospheric background fields is valid). Liuzzo et al. (2019) found that a similar shielding mechanism (caused by electric field voids) generates a reduction in accessibility for energetic *ions* (see Section 3.4 of that work). However, since the gyroradii of energetic ions at a given energy are much larger than those of energetic electrons, the electric field depletions that shield ions are as large as Callisto; i.e., they are much more extended than the void visible in Fig. 8. Such a large void in the electric field is generated by mass-loading from Callisto's ionosphere and in the associated Alfvén wings (see Section 3.3 for further details).

For *back-traced* electrons with energies $E \geq 10^3$ keV, the accessibility remains below $\lambda < 100\%$ everywhere (see panels 7(c)–7(e)). As with Run #1, electron gyroradii of $r_g > 0.05R_C$ allow *back-traced* electrons to gyrate into the hard cutoff for forbidden electrons soon after initialization, again causing a "switch-like" decrease in the global accessibility between panels 7(b) and 7(c), while leaving the overall pattern qualitatively unchanged. With increasing energy (e.g., for $E = 10^4$ keV, see panel 7(d)), electron gyroradii surpass the extension of the electric field void above Callisto's north pole, and accessibility values near this region approach $\lambda \approx 50\%$. At the highest energy considered, electron gyroradii exceed $1R_C$; i.e., the relative size of the Callisto obstacle—compared to electron scales—decreases (see panel 7(e)), and the accessibility map approaches quasi-homogeneity.

Overall, the accessibility maps for Run #2 show that, due to small

electron gyroradii, even small-scale structures in the electromagnetic fields have a tremendous influence on energetic electron dynamics near Callisto and can not be neglected.
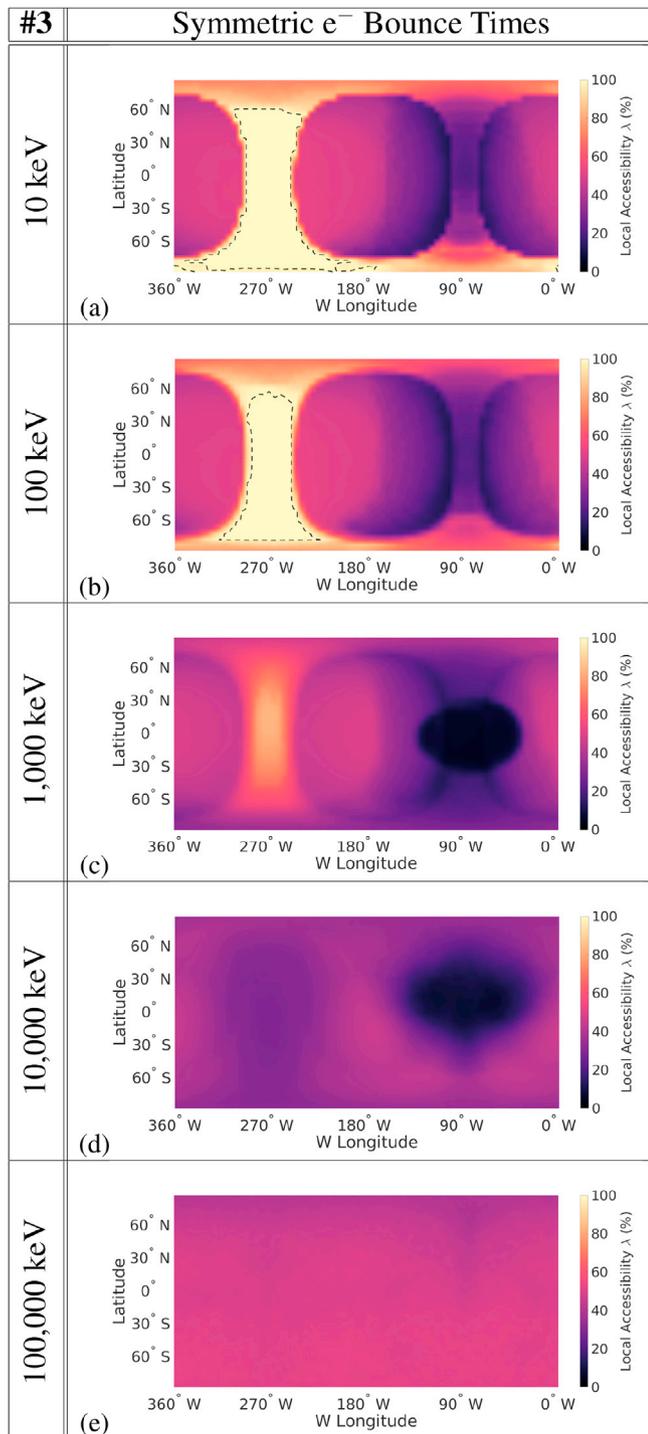
3.3. Energetic electron accessibility: plasma interaction with Callisto's ionosphere alone (Run #3)

Displayed in Fig. 9 is the accessibility of Callisto to energetic electrons for the electromagnetic fields of Run #3, a strong plasma interaction with Callisto's ionosphere alone. This configuration corresponds to Callisto located near the center of Jupiter's magnetospheric current sheet, where the moon's induced field vanishes as observed during, e.g., the Galileo C23 flyby (Liuzzo et al., 2017). Hence, Callisto's induced dipole is *not* included in Run #3.

At the lowest energies considered, panels 9(a) and 9(b) show two distinct features in the electron accessibility patterns. The first feature are two quasi-circular regions with accessibility values of $\lambda \approx 50\%$ that drop to a value of only $\lambda \approx 10\%$ in the moon's wakeside hemisphere. These regions are centered in Callisto's equatorial plane at 0° W and 180° W longitude and envelop large portions of the moon's Jupiter-facing and Jupiter-averted hemispheres. The extent of each region is nearly 150° in longitude *and* latitude, and together they cover nearly 80% of the starting grid. The second distinct feature in panels 9(a) and 9(b) is a stripe of high accessibility (with $\lambda \approx 100\%$) in Callisto's orbital trailing hemisphere near 270° W longitude that extends to latitudes poleward of 60° N and S. This second feature was also present in the ramside accessibility pattern at low electron energies in Run #2.

The two quasi-circular features in Callisto's Jupiter-facing and Jupiter-averted hemispheres coincide with the regions where the Alfvénic fluxtubes are "anchored" to the moon's ionosphere. This is visible in Fig. 10, which illustrates the structure of Callisto's magnetic environment as well as the accessibility map of 10 keV electrons for Run #3. The draped field lines are color-coded with values of the B_x component, with $B_x > 0$ in red and $B_x < 0$ in blue. It is evident from Fig. 10 that the two depletions (where $\lambda \approx 50\%$) coincide with the "anchor regions" of the Alfvénic fluxtubes. The field lines in the Alfvén wings are closed *below the starting grid* through Pedersen and Hall currents in Callisto's ionosphere (Liuzzo et al., 2015).

In Run #3, Callisto is embedded in an electric field void caused by slowly moving ionospheric plasma. This $|\mathbf{E}| \approx 0$ bubble extends multiple R_C from the moon in each direction; see Fig. 3 of Liuzzo et al. (2019) for the electric field configuration of Run #3 or Liuzzo et al. (2015) for more detailed discussion. Hence, *back-traced* electrons initialized within this bubble travel along the draped magnetic field lines without being transported toward upstream by the $\mathbf{E} \times \mathbf{B}$ drift. Since the gyroradii of electrons with $E \leq 100$ keV are on the order of only $10^{-2}R_C$, their motion

#3 | Symmetric e⁻ Bounce Times

Fig. 9. Energetic electron accessibility at select energies for the electromagnetic fields of Run #3, a plasma interaction with Callisto's ionosphere alone (see Table 1), using "symmetric" bounce times and azimuthal displacements. See Fig. 4 and the text for further description.

within this extended electric field void can mainly be described as a pure translation along the magnetic field. Therefore, if an electron (initialized within one of the "anchor regions") translates along the draped magnetic field lines *toward* Callisto, it will inevitably re-encounter the cutoff at $|\mathbf{r}| = 1.05R_C$ and become forbidden. This outcome occurs for 50% of the back-traced electrons injected within each "anchor region." Thus, only *half* of the electrons initialized within these regions travel *away* from Callisto, and the accessibility value here can reach a maximum value of only $\lambda = 50\%$.
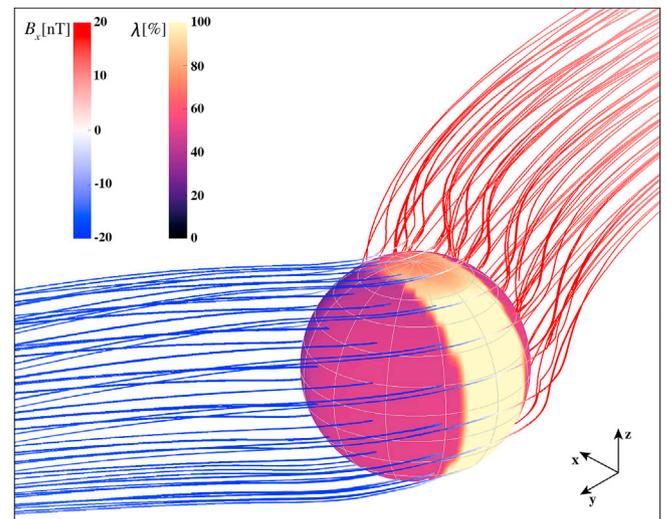
Fig. 10. Magnetospheric field line draping and 10 keV electron accessibility pattern for Run #3. Field lines near Callisto are color-coded to show (red) positive and (blue) negative values of B_x, with regions of $B_x = 0$ in white (see also Fig. 1(c)), and the accessibility map on the starting grid is identical to Fig. 9(a). The viewing geometry is from a point located upstream of Callisto in its northern, Jupiter-facing hemisphere. (For interpretation of the references to color in this figure legend, the reader is referred to the Web version of this article.)

At energies $E \leq 100$ keV, all *back-traced* electrons are displaced toward upstream after bouncing with azimuthal displacements r_{eq} that range from approximately $10R_C \leq r_{eq} \leq 20R_C$ (see Fig. 2). Hence, if a *back-traced* electron leaves the AIKEF simulation domain by translating along the magnetic field lines, it will *not* return to Callisto's local environment; i.e., its trajectory is "allowed." However, this occurs only for electrons that are initialized at starting positions upstream of 20° W and 160° W longitude. Indeed, the electron accessibility pattern in Callisto's leading hemisphere displays a longitudinal decrease in accessibility from $\lambda \approx 50\%$ down to values of $\lambda \approx 10\%$ when moving toward 90° W longitude within both "anchor regions." At longitudes further into Callisto's leading hemisphere, the electrons are injected into the wakeside magnetic depletion region due to mass-loading from Callisto's ionosphere (see Fig. 1(g)). When such electrons attempt to leave the region of reduced $|\mathbf{B}|$ at Callisto's wakeside, they first need to pass through regions of stronger field and they are reflected (up to multiple times) by the magnetic mirror force. Such electrons may eventually re-encounter the hard cutoff for forbidden electrons. Hence, the escape of electrons along the draped magnetic field lines is partially prevented by the inhomogeneous field *magnitude* near Callisto which acts as a "magnetic mirror" (similar to the induced dipole field in Runs #1 and #2, see Fig. 5). Thus, in order to understand the decrease in λ (within the anchor regions) when moving toward Callisto's wakeside, it is important to recognize the occurrence of two competing effects: field line draping corresponding to a strong B_x component (see Fig. 1(c)) facilitates the escape of *back-traced* electrons from Callisto, whereas a decreasing magnetic field magnitude at the wakeside (see Fig. 1(g)) prevents such electrons from escaping.

Centered around 270° W longitude is again a stripe of high accessibility with $\lambda \approx 100\%$. Since electrons initialized near this meridian are located within the electric field void, they mainly translate along the magnetic field lines. However, in this region, the magnetic field is nearly tangential to Callisto (where $B_x \approx 0$, see the white segments of the field lines in Fig. 10). Newly-injected, *back-traced* electrons are therefore able to leave Callisto's local interaction region by traveling parallel *or* antiparallel to the magnetic field without immediately encountering the cutoff and becoming forbidden (similar to electrons with $E \leq 100$ keV in Run #1, cf. Fig. 4). Thus, the number of electrons that may potentially have allowed trajectories is twice as high as in the "anchor regions."

Indeed, since *back-traced* electrons with $E \leq 100$ keV are always displaced on the order of $10R_C$ toward upstream after bouncing, they can never re-encounter the starting grid after mirroring and λ near 270° W longitude approaches 100%. In Callisto's leading hemisphere, a similar stripe of slightly enhanced λ forms between the two "anchor regions" where the magnetic field is tangential to the moon. At these locations, a certain fraction of energetic electrons is again able to leave Callisto's plasma interaction region parallel or anti-parallel to **B**. However, due to the confining effect of the wakeside "magnetic mirror," λ does not reach 100%.

This mechanism of energetic particles traveling along the field lines within Callisto's Alfvén wings was also found to occur for energetic *ions* of the same energy in the fields of Run #3 (see Fig. 8 of Liuzzo et al. (2019)). However, the stripe of enhanced accessibility near 270° W longitude (see Fig. 9(a)) was *not* present in the accessibility pattern of energetic ions. Instead, Liuzzo et al. (2019) found that a region of *reduced* ion accessibility forms in Callisto's trailing hemisphere. This depletion occurs because, in addition to their translational motion along the magnetic field, energetic ions gyrate with $r_g \approx 1R_C$ around the (locally tangential) field near 270° W longitude. Liuzzo et al. (2019) showed that these large gyroradii cause back-traced ions to gyrate into the starting grid soon after initialization, thereby generating a band of reduced accessibility upstream.

These effects are also likely present at Europa, but to a slightly lesser degree. Similar to at Callisto, Nordheim et al. (2018) found the apices of Europa's leading and trailing hemispheres (near 90° W and 270° W longitude) to be most accessible to energetic electrons. These authors calculated the precipitation pattern of electrons onto Europa by comparing their bounce times against the convection times of the "guiding" magnetospheric field lines through the moon's local environment. However, their model assumed the ambient magnetic field to be homogeneous; i.e., these authors considered neither Europa's induced dipole field nor the deceleration and deflection of the magnetospheric field lines due to mass loading near the moon. While weaker than at Callisto, Europa's interaction with the magnetospheric plasma still generates perturbations that are approximately 20% of the background magnetic field strength (see, e.g., Blöcker et al. (2016); Arnold et al. (2019)). Nevertheless, a qualitative similarity of our results to those of Nordheim et al. (2018) can be expected at (and *only* at) 90° W and 270° W longitude, since even a homogeneous field is tangential to the surface of Europa near these locations.

When increasing *electron* energy up to $E = 10^3$ keV (see panel 9(c)), another distinct feature in the accessibility pattern forms: an elliptical depletion region of $\lambda \approx 0$ is carved out around Callisto's leading apex (near 90° W longitude). Due to their larger gyroradii at this energy ($r_g > 0.1R_C$), electrons initialized within the reduced magnetic field downstream of Callisto (see Fig. 1(g)) gyrate into the starting grid soon after initialization while translating through the electric field void that envelops the moon. Additionally, their azimuthal displacements decrease to values below approximately $|r_{eq}| < 4R_C$ (see, e.g., Fig. 2(b)). This effect causes bouncing electrons initialized near 90° W to be re-injected along field lines that still intersect Callisto, thereby reducing the accessibility in this region to $\lambda \approx 0$%. At even higher energy (Fig. 9(d)), the role of reduced $|r_{eq}|$ and enhanced electron gyroradii in generating the depletion at the leading apex is even more pronounced. However, the growth of this depletion region is non-monotonic with increasing energy. At the lowest energies considered ($E \leq 10^2$ keV), this depletion is absent, only forming at intermediate energies (10^3 keV $\leq E \leq 10^4$ keV). At the highest energy considered when electron gyroradii become $r_g \gg R_C$, this cavity again vanishes (see panel 9(e)) as electrons are able to gyrate around Callisto and the map approaches quasi-homogeneity.

3.4. Energetic electron accessibility: plasma interaction with Callisto's induced dipole and ionosphere (Run #4)

The accessibility of Callisto to energetic electrons in the electro-

magnetic fields of Run #4 is shown in Fig. 11. These fields correspond to Callisto being located at intermediate distances h_{cs} to the center of Jupiter's magnetospheric current sheet. At these distances, a strong interaction of the thermal magnetospheric plasma with Callisto's induced dipole *and* ionosphere is present, as was observed during the Galileo C10 flyby (Liuzzo et al., 2016).

The accessibility patterns of electrons at all energies show a striking resemblance to those in the electromagnetic fields of Run #1 (cf. Fig. 4).
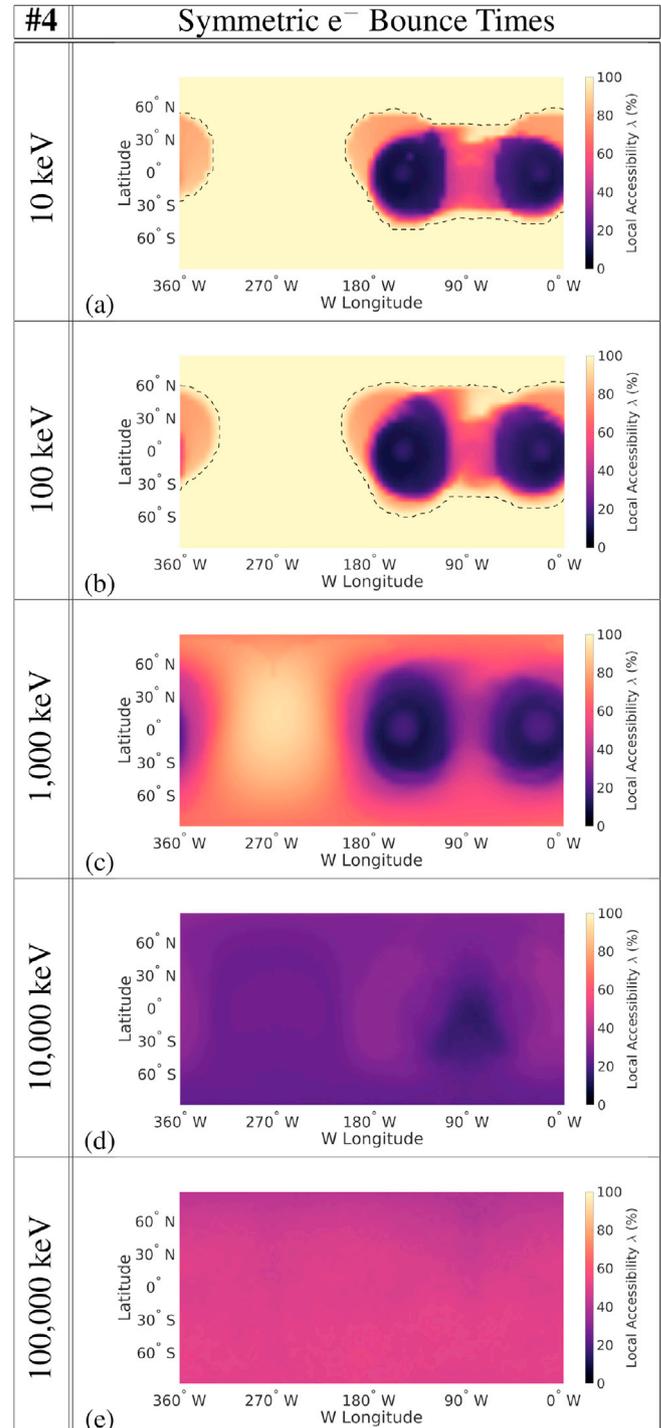

Fig. 11. Energetic electron accessibility at select energies for the electromagnetic fields of Run #4, a strong plasma interaction with Callisto's ionosphere *and* induced dipole (see Table 1). The accessibilities correspond to "symmetric" bounce times and azimuthal displacements. See Fig. 4 and the text for further description.

At energies $E \leq 100$ keV (panels 11(a) and 11(b)), two circular regions with $\lambda \approx 10\%$ form near the equator at 0° W and 180° W longitude and extend to latitudes of 30° N and S. Compared to Run #1, these regions of reduced accessibility are slightly shifted into the leading hemisphere, as the locations of minimum $|\mathbf{B}|$ are displaced toward downstream by the plasma interaction similar to Run #2 (see Fig. 1 and also Liuzzo et al. (2019)). These λ depletions are connected in the leading hemisphere by a region of slightly enhanced accessibility, centered at 90° W and extending to latitudes of 30° N and S (where $\lambda \approx 50\%$). Everywhere else on the starting grid, the accessibility approaches values of $\lambda \approx 100\%$. Thus, despite the strong plasma interaction, the presence of Callisto's induced dipole shrinks the regions of reduced electron accessibility from covering 80% of the starting grid in Run #3 to about 40% in Run #4. This is similar to Run #1 which considered only a very weak interaction with the induced field.

At altitudes above $0.5R_C$, field line draping dominates the magnetic signatures in Run #4 and the fields there are similar to Run #3 (see, e.g., Fig. 1 and Liuzzo et al. (2016)). Yet, despite the similarities of the large-scale electromagnetic field perturbations, the effect of the draping on energetic electron accessibility is remarkably less drastic when Callisto's induced field is present. The pronounced, broad λ depletions within the two "anchor regions" of the Alfvénic flux tubes visible in the leading hemisphere for Run #3 have drastically shrunk in Run #4 (cf. Fig. 9 with Fig. 11). This is because close to the surface of Callisto's leading hemisphere, the magnetic signatures are dominated by the induced magnetic field, nearly unobscured by any plasma currents. This region was called the quasi-dipolar "core region" by Liuzzo et al. (2016). Hence, near Callisto's wakeside surface, the magnetic field is nearly the same as in Run #1. For this reason, the electron accessibility pattern in this hemisphere can be explained in analogy to Fig. 4. *Back-traced* electrons that are injected slightly downstream of the "poles" of Callisto's induced field are initially exposed to a region of reduced $|\mathbf{B}|$ and are confined within this region by the same "magnetic bottle" effect as in Runs #1 and #2, resulting in a decrease in λ. However, closer to Callisto's leading apex, the superposition of the induced field with $\mathbf{B}_0$ results in an enhanced field magnitude, thereby allowing more electrons to escape and slightly increasing λ near 90° W longitude (analogous to Run #1). The accessibility pattern in Callisto's leading hemisphere is therefore governed by this superposition of the induced and background field near the surface, irrespective of the Alfvénic perturbations that manifest at larger distances to the moon.

In Callisto's trailing hemisphere between 180° W and 360° W longitude, λ reaches 100% nearly everywhere for $E \leq 100$ keV (see Fig. 11(a) and (b)), as *back-traced* electrons are again able to leave the interaction region parallel or anti-parallel to the piled-up magnetic field. Because the displacements r_{eq} of such electrons are always toward upstream, they never encounter the hard cutoff after bouncing. Hence, similar to Runs #1 through #3, tangential magnetic field lines within the upstream pileup region generate a broad segment of enhanced electron accessibility. At higher energies, an increase in electron gyroradii causes the familiar "switch-like" reduction in the accessibility values (panel 11(c)), while the qualitative shape of the accessibility pattern is maintained. At the highest energies, the maps again approach quasi-homogeneity (panels 11(d) and 11(e)).

In comparing the accessibility pattern of Run #4 with those of Runs #1 through #3, Fig. 11 illustrates that in a *forward-tracing* picture, the shape of the magnetic field lines along which electrons travel during their approach to Callisto is *not* relevant in generating key features of the precipitation patterns. Rather, the most important factor is the magnetic field close to the moon below altitudes of $0.5R_C$. If Callisto's induced dipole is present, then electrons approaching the leading hemisphere must penetrate the quasi-dipolar "core region" in order to precipitate. Although the extension of this region is small compared to Callisto, it is still *much* larger than the scales on which energetic electron dynamics occur. Therefore, despite the drastically different strengths of plasma currents, the precipitation patterns of energetic electrons are similar for

Runs #1 and #4. Hence, signatures of the Alfvénic interaction with Callisto's ionosphere are clearly identifiable in energetic electron accessibility patterns only near the center of Jupiter's magnetospheric current sheet ($h_{cs} = 0$) where the induced field vanishes.

In summary, even in the case of a strong thermal plasma interaction, Callisto's induced field partially protects the moon's Jupiter-facing and Jupiter-averted apices from irradiation by energetic electrons. Since the induced field vanishes only briefly during each synodic rotation period (specifically, when Callisto is near the center of the Jovian current sheet where the magnetic moment merely flips its direction), this protection mechanism likely does *not* average out over a full Jovian rotation. This mechanism would be much weaker, however, at Europa. In contrast to Callisto, the magnetospheric field near Europa is dominated by its strong north/south component, which can *not* be canceled by the induced dipole at any point on the surface (Zimmer et al., 2000).
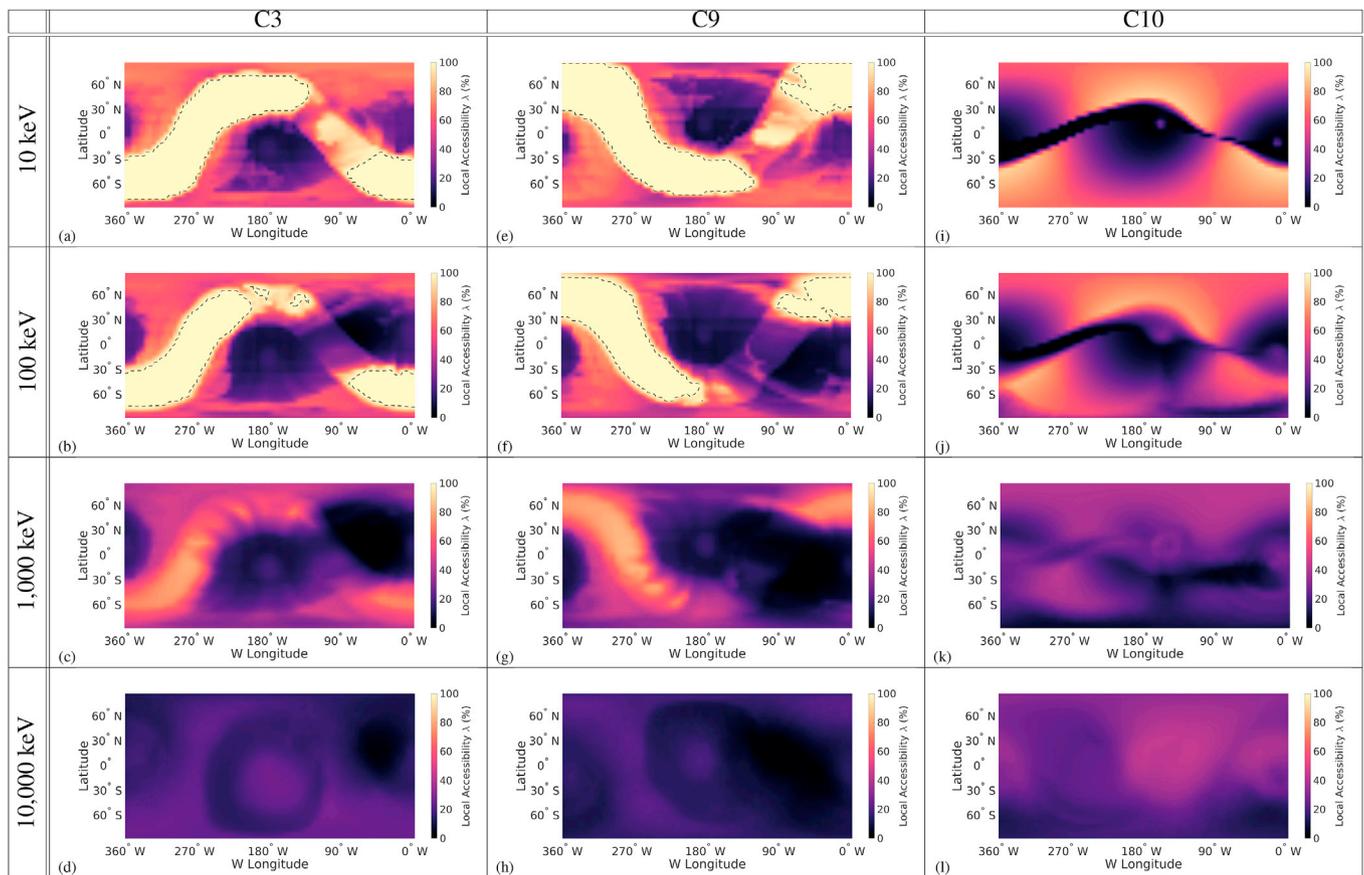
4. Energetic electron accessibility of Callisto during the Galileo C3, C9, and C10 flybys

Throughout the course of Galileo's eight year mission at Jupiter, the spacecraft performed eight targeted flybys of Callisto. However, Callisto's inductive response was detected only during the first three flybys, denoted C3, C9, and C10 (Liuzzo et al., 2017). The precipitation patterns of energetic *ions* during these three flybys have been studied by Liuzzo et al. (2019), using the stationary electromagnetic field output from the AIKEF hybrid model. Thus, to complement their findings, we investigate the accessibility patterns of energetic *electrons* during these same three encounters. During C3, Callisto was located at $h_{cs} \approx 3.2R_J$ (i.e., far *above* the center of Jupiter's magnetospheric current sheet), while during C9, Callisto was at $h_{cs} \approx -3.5R_J$ (i.e., far *below* the center). During the C10 flyby, Callisto was located at an intermediate distance below the center of Jupiter's current sheet, with $h_{cs} \approx -2.5R_J$. The AIKEF output for C3, C9, and C10 has been discussed in our preceding publications. Thus, for the complete set of upstream parameters used in the hybrid simulations for these three flybys, the reader is referred to Liuzzo et al. (2015) (for C3 and C9) and Liuzzo et al. (2016) (for C10).

Near closest approach of C3, the magnetospheric background field was $\mathbf{B}_0 = [-2.4\hat{\mathbf{x}} - 31.7\hat{\mathbf{y}} - 10.8\hat{\mathbf{z}}]$ nT; i.e., the field was oriented *away* from Jupiter. During C9, however, the background field was oriented *toward* Jupiter with $\mathbf{B}_0 = [+3.3\hat{\mathbf{x}} + 33.9\hat{\mathbf{y}} - 9.4\hat{\mathbf{z}}]$ nT. Since Callisto was located at large $|h_{cs}|$ values during these two flybys, only weak plasma interaction currents were present (e.g., Zimmer et al. (2000); Liuzzo et al. (2015)) and the setup of our C3 and C9 simulations best corresponds to Run #2 (see Section 3.2).

Fig. 12 displays the accessibility of Callisto to energetic electrons during the C3 (panels 12(a)–12(d)), C9 (panels 12(e)–12(h)), and C10 (panels 12(i)–12(l)) flybys. These accessibility maps use the specific location of Callisto within Jupiter's magnetosphere during the respective encounter (i.e., the moon's System III longitude and local time; see, e.g., Table 1 in Liuzzo et al. (2015)) to calculate the half bounce times and azimuthal displacements of energetic electrons. Hence the half bounce times are "asymmetric:" for C3 ($h_{cs} > 0$), electrons that mirror in Jupiter's *northern* hemisphere bounce much faster than electrons mirroring in the *southern* hemisphere, while the opposite is true for C9 and C10 ($h_{cs} < 0$).

For the C3 and C9 encounters, a broad ribbon of enhanced accessibility ($\lambda \approx 100\%$) wraps around Callisto for electrons with energies $E \leq 100$ keV (yellow regions in panels 12(a) and 12(b) for C3, or 12(e) and 12(f) for C9). Within this ribbon in Callisto's trailing hemisphere, the magnetic field is nearly tangential to the starting grid, thereby facilitating escape of *back-traced* electrons (similar to Runs #2 and #3). When comparing the maps between C3 and C9, these ribbons of high accessibility appear mirrored about Callisto's equatorial plane. This effect occurs because the background field vectors during C3 and C9 were inclined against each other by 145°, causing the orientation of the background field with respect to the induced magnetic moment to

Fig. 12. Accessibility of Callisto to energetic electrons during the (a)–(d) C3, (e)–(h) C9, and (i)–(l) C10 Galileo flybys. These maps consider "asymmetric" bounce times and azimuthal displacements that correspond to Callisto's System III longitude and local time in the Jovian magnetosphere during each flyby. Maps for electrons with $E = 10^5$ keV are omitted, as the patterns already display a homogeneous value of $\lambda \approx 50\%$. See Fig. 4 and the text for further discussion.

strongly differ between the two simulations. These differences in the magnetic field near the starting grid alter the locations where magnetic field lines are tangential, thereby resulting in rotated accessibility patterns.

Centered in Callisto's equatorial plane and near 0° W and 180° W longitude are two regions of reduced accessibility for C3 and C9; i.e., these $\lambda \approx 0$ features flank either side of the high-accessibility ribbon (see Fig. 12(a) and (b), 12(e), and 12(f)). Again, these depletions are mainly generated by Callisto's induced dipole that causes a "magnetic bottle" effect for the *back-traced* electrons (as in Run #2), with a weak contribution of the Alfvén wings that allow electrons to escape near the edges of these features (as in Run #3). Although Callisto's induced dipole never exactly cancels $\mathbf{B}_0$ during these flybys (due to the non-zero $B_{z,0}$ component), these depletions still form where $|\mathbf{B}|$ is minimized. In the equatorial plane, this occurs near 0° and 180° W longitude, since $\mathbf{M}_{ind}$ is inclined against the y-axis by only 5° during these flybys. However, these λ depletions are slightly shifted into the leading hemisphere due to the (weak) plasma interaction during C3 and C9 (see also Run #2).

Near the apex of Callisto's leading hemisphere, *back-traced* electrons are initialized within a region of magnetic field that is enhanced compared to the background value, and they are thus unlikely to remain within the "magnetic bottle" close to the moon formed by the locally perturbed fields. This generates an enhancement in λ within the ribbon of high accessibility. At higher energies of 10^3 keV $\leq E \leq 10^4$ keV (panels 12(c) and 12(d) for C3, or panels 12(g) and 12(h) for C9), λ again drops to below 100% everywhere and the features present below 100 keV begin to blur. At energies of $E = 10^5$ keV, the maps would become nearly homogeneous (and thus, are not shown here).

At the time of the C10 flyby, Callisto was located closer to the center of the Jovian magnetospheric current sheet than during C3 or C9. The

magnetospheric background field near closest approach of C10 mainly pointed toward Jupiter, with $\mathbf{B}_0 = [0.0\hat{\mathbf{x}} + 29.0\hat{\mathbf{y}} - 11.2\hat{\mathbf{z}}]$ nT. Galileo measurements obtained during C10 suggest a complex system of plasma currents generated by the magnetospheric interaction with the moon's induced field *and* mass-loading from its ionosphere (Gurnett et al., 2000; Liuzzo et al., 2016). Hence, Callisto's electromagnetic environment during C10 was qualitatively similar to the electromagnetic fields of Run #4 in this study (see Section 3.4).

Panels 12(i)–12(l) illustrate energetic electron accessibility during the C10 flyby. Again, similar to the other flybys, two prominent depletion regions form near 0° W and 180° W longitude. These are mainly generated by Callisto's induced field causing a "magnetic bottle" effect in these regions near the moon's "magnetic poles" ($\mathbf{M}_{ind}$ was aligned with $-\hat{\mathbf{y}}$ since $B_{x,0} = 0$). These depletions are also associated, to a lesser degree, with the "anchor regions" of the moon's Alfvénic flux tubes which—despite the non-zero $B_{z,0}$ component—still cover large portions of Callisto's Jupiter-facing and Jupiter-averted hemispheres (see Fig. 2(a) of Liuzzo et al. (2016)). In contrast to C3 and C9, however, the accessibility values remain below 100% at all locations and for all energies shown. At the highest energy shown (panel 12(l)), the pattern again becomes quasi-homogeneous, and at $E = 10^5$ keV, accessibility reaches a homogeneous value of $\lambda \approx 50\%$ everywhere (and is therefore omitted from Fig. 12).

In summary, many of the features from the idealized electromagnetic field geometries presented in Runs #1 through #4 are still visible in the accessibility patterns of C3, C9, and C10. However, the patterns are stretched and rotated around the starting grid, consistent with the orientation of the magnetospheric background field and its non-zero inclination against the induced dipole moment.

The only published electron energy spectrogram obtained during a Callisto flyby is from C3 (see, e.g., Fig. 3 of Cooper et al. (2001)). This spectrogram displays the intensity of electron fluxes near Callisto taken over a 5-h period between 11:00 and 16:00 on 04 November 1996. Since the wake crossing of Galileo during C3 was much shorter than this 5-h time frame, the local influence of Callisto's thermal plasma interaction on the electron spectrogram was likely averaged out. Hence, we consider this spectrogram to be a realistic representation of the ambient energetic electron distribution during the encounter.

In analogy to Liuzzo et al. (2019), we use this measured, ambient electron spectrogram $I_0(E)$ (as obtained from Cooper et al. (2001)) to calculate the intensity of energetic electron fluxes $I_{TOA}(E)$ onto different locations at the top of Callisto's atmosphere during C3. To do so, we assume that the measured ambient distribution is isotropic and spatially homogeneous (i.e., that all impinging electrons stem from the same distribution). We then multiply these intensities $I_0(E)$ by the accessibility values $\lambda(E)$ calculated for the C3 flyby (see Fig. 12) to obtain the energy-dependent intensity of the electron flux $I_{TOA}(E) = \lambda(E) \cdot I_0(E)$ for a specific point on the starting grid, similar to Regoli et al. (2016) and Liuzzo et al. (2019). Here, we assume that the changes in $\lambda(E)$ between the discrete energies simulated in this study are approximately linear.

The solid black line in Fig. 13 displays the intensity of the ambient electron flux $I_0(E)$ near Callisto, as measured during the Galileo C3 flyby (Cooper et al., 2001). Since the EPD instrument was only able to measure electrons below energies of approximately $E \leq 700$ keV, the dashed segment of the black line displays electron fluxes up to energies of $E \approx 3,000$ keV, obtained from the model of Divine and Garrett (1983) and presented in Cooper et al. (2001). The fluxes $I_{TOA}(E)$ incident onto the top of Callisto's atmosphere are also included in Fig. 13 for four equatorial locations: (violet) 0° W, (pink) 90° W, (orange) 180° W, and (yellow) 270° W longitude. As can be seen in Fig. 12(a)–(d), λ is substantially different at these four positions.
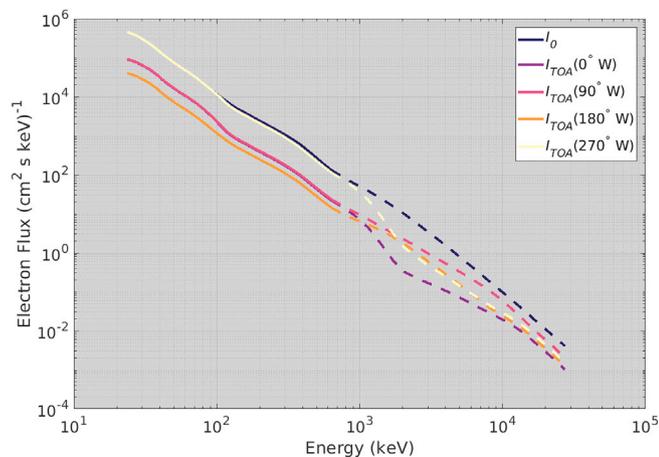
Fig. 13. Intensity of energetic electron flux near Callisto during the Galileo C3 flyby. The solid black $I_0(E)$ line depicts the averaged, measured intensity of energetic electron flux for energies $E \leq 700$ keV between 11:00 and 16:00 on 04 November 1996, obtained from Fig. 3 of Cooper et al. (2001). Since the EPD did not measure electrons with energies greater than $E \approx 700$ keV, the dashed black line uses the Divine and Garrett (1983) model for electron fluxes extended up to energies of $E = 3,000$ keV (see Cooper et al. (2001) for more details). The various $I_{TOA}(E) = \lambda(E) \cdot I_0(E)$ curves correspond to the energetic electron flux onto the top of Callisto's atmosphere at four equatorial positions: (violet) 0° W, (pink) 90° W, (orange) 180° W, or (yellow) 270° W longitude. These curves consider the reduction of the ambient flux as a result of the thermal plasma interaction with Callisto's induced dipole (see Section 4). To discriminate between the electron fluxes observed by EPD and the fluxes extended up to higher energy from Divine and Garrett (1983), we also display our $I_{TOA}(E)$ curves in solid or dashed lines, respectively. (For interpretation of the references to color in this figure legend, the reader is referred to the Web version of this article.)

As visible in Fig. 13, the precipitation of energetic electrons varies drastically between these four points, most noticeably below approximately $E \leq 10^3$ keV. Differences in electron accessibility λ at a given energy cause the fluxes to vary by up to an order of magnitude between different locations at the top of the atmosphere. While nearly all of the upstream distribution below 10^3 keV can precipitate onto Callisto's equatorial trailing hemisphere (yellow line, representing 270° W longitude), the electron fluxes at the other three apices are drastically reduced. These inhomogeneous fluxes likely generate a non-uniform ionization pattern of Callisto's atmosphere and, if a non-negligible amount of electrons can penetrate through the atmosphere, may cause uneven sputtering of the moon's surface. However, a detailed investigation of these effects is the subject of a future study. At energies above 10^4 keV in Fig. 13, the accessibility patterns reach quasi-homogeneity and the four I_{TOA} curves converge against each other (see also the accessibility pattern in Fig. 12). However, the intensity of the ambient electron flux $I_0(E)$ is reduced by nearly nine orders of magnitude compared to values at the lowest energies.

5. Summary and concluding remarks

This study has analyzed the dynamics of energetic electrons (10^1 keV $\leq E \leq 10^5$ keV) near Callisto for four distinct scenarios of the thermal magnetospheric plasma interaction with the moon's induced dipole and/or its ionosphere. Our findings have also been applied to investigate the precipitation of energetic electrons onto the top of Callisto's atmosphere at the times of the Galileo C3, C9, and C10 flybys.

Our results have shown that the precipitation patterns of energetic electrons are highly susceptible to the local electromagnetic field perturbations near Callisto; any simplifying assumption of homogeneous fields near the moon is therefore *not* adequate to understand energetic electron dynamics. When Callisto is near the center of the Jovian current sheet, field line draping and formation of Alfvén wings reduces the accessibility of the moon's Jupiter-facing and Jupiter-averted hemispheres to energetic electrons. At large distances to the center of the sheet, Callisto's induced dipole drastically reduces electron accessibility in the same regions. Thus, these two apices are (partially) protected from energetic electron impacts throughout an entire synodic rotation. As a result, the ionization of Callisto's atmosphere by precipitating electrons is likely inhomogeneous, and these differences may also generate a non-uniform erosion pattern across the moon's surface. Unlike energetic *ions*, the rapid half-bounce period of energetic *electrons* may cause them to return to the locally perturbed electromagnetic fields near Callisto. Such bouncing electrons may have multiple opportunities to precipitation onto Callisto and may impose a slight, additional inhomogeneity on the precipitation patterns.

Hints of non-uniform electron precipitation patterns at Callisto have indeed been observed by the EPD instrument during at least one Galileo flyby: displayed in Fig. 14(a) is a time series of electron counts by the E0 channel (measuring 15 keV $\leq E \leq 29$ keV electrons) during C10, approximately ± 30 minutes surrounding closest approach. Highlighted in cyan is the 2-min period between 00:21 and 00:23 during which E0 (and multiple other EPD channels) detected a significant depletion in electron count rates. Included in panel 14(b) is the accessibility pattern of 10 keV electrons during the C10 flyby (see also Fig. 12(i)). Among the discrete electron energies we modeled, $E = 10$ keV is closest to the energy range of E0, and below 10^3 keV, the modeled pattern changes only quantitatively (see panels 12(i)–12(l)). Projected onto this map is the C10 flyby trajectory while the spacecraft was located within Callisto's geometric plasma shadow (i.e., the cylinder defined by $y^2 + z^2 \leq R_C^2$ and $x > 0$). As can be seen, the (cyan) depletion in count rates for the E0 channel in panel 14(a) coincides with a region of reduced accessibility in panel 14(b) during the outbound segment of the C10 flyby trajectory. Similar depletions may also be observed during future Callisto flybys from the upcoming
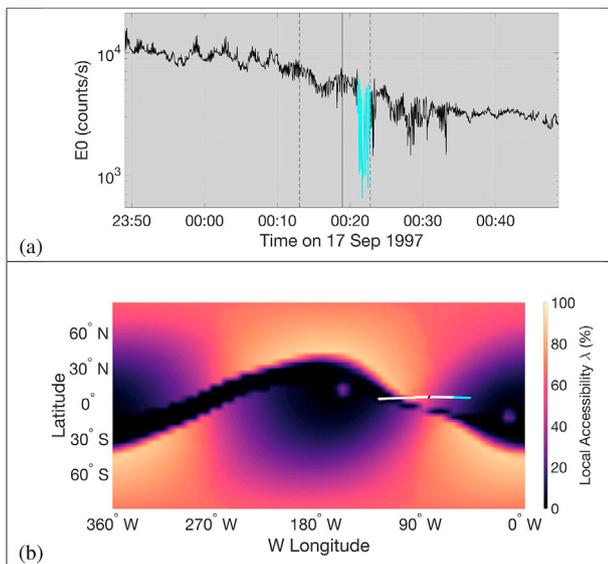
Fig. 14. (a) Electron counts per second measured by the E0 channel ($15\,\text{keV} \leq E \leq 29\,\text{keV}$ electrons) of EPD during the Galileo C10 flyby. The solid vertical line corresponds to closest approach at 00:18:55 on 17 September 1997, and the dashed vertical lines denote Callisto's geometric plasma shadow ($y^2 + z^2 \leq R_C^2$ and $x > 0$). The sudden decrease in count rates observed within Callisto's geometric plasma shadow is highlighted in cyan. Data was obtained from the *Planetary Data System*. (b) 10 keV electron accessibility pattern during C10, as also shown in Fig. 12(i). Included in white is the projection of the flyby trajectory onto the starting grid while Galileo was located within Callisto's geometric plasma shadow. The black segment of this trajectory marks closest approach, whereas the cyan segment denotes the observed count rate decrease near the outbound edge of the plasma shadow, corresponding to the identical cyan region in panel (a). (For interpretation of the references to color in this figure legend, the reader is referred to the Web version of this article.)

JUpiter ICy moons Explorer mission (Grasset et al., 2013) by the *Particle Environment Package*. However, further understanding of the observed depletion in the Galileo C10 EPD data would require modeling electron precipitation *into the EPD instrument* in a similar fashion as Kotova et al. (2015) did for Cassini's energetic particle detector during flybys of Rhea and Dione. This is the subject of a future study.

Finally, besides Fig. 3 of Cooper et al. (2001), an additional electron spectrogram obtained during the C3 flyby was presented in Fig. 14 of Mauk and Saur (2007). That spectrogram is a snapshot of the energetic electron intensities $I(E)$ during the brief time frame when Galileo was located *within* Callisto's wake. While the fluxes at energies near $E \approx 10$ keV in the spectrogram of Mauk and Saur (2007) are a factor of four smaller than in the data set provided by Cooper et al. (2001), the $I(E)$ curves in those two studies are nearly indistinguishable at higher energies. Whether or not these discrepancies near $E \approx 10$ keV are caused by the (weak) electromagnetic perturbations in Callisto's wake during C3 will be investigated in a follow-up study.

Acknowledgments

References

Arnold, H., Liuzzo, L., Simon, S., 2019. Magnetic signatures of a plume at Europa during the Galileo E26 flyby. Geophys. Res. Lett. 46, 1149–1157.

Belcher, J.W., 1983. The low-energy plasma in the Jovian magnetosphere. Phys. Jovian Magnetosphere 1, 68–105.

Bhattacharyya, D., Clarke, J.T., Montgomery, J., Bonfond, B., Gérard, J.-C., Grodent, D., 2017. Evidence for auroral emissions from Callisto's footprint in HST UV images. J. Geophys. Res.: Space Phys. 123, 364–373. https://doi.org/10.1002/2017JA024791.

Blöcker, A., Saur, J., Roth, L., 2016. Europa's plasma interaction with an inhomogeneous atmosphere: development of Alfvén winglets within the Alfvén wings. J. Geophys. Res.: Space Phys. 121, 9794–9828.

Boris, J.P., 1970. Relativistic plasma simulation-optimization of a hybrid code. In: Proc. 4th Conf. Num. Sim. Plasmas, pp. 3–67.

Carlson, R.W., 1999. A tenuous carbon dioxide atmosphere on Jupiter's moon Callisto. Sci. 283, 820. https://doi.org/10.1126/science.283.5403.820.

Cassidy, T., Paranicas, C., Shirley, J., Dalton III, J., Teolis, B., Johnson, R., Kamp, L., Hendrix, A., 2013. Magnetospheric ion sputtering and water ice grain size at Europa. Planet. Space Sci. 77, 64–73. https://doi.org/10.1016/j.pss.2012.07.008.

Connerney, J.E., Acuña, M.H., Ness, N.F., Satoh, T., 1998. New models of Jupiter's magnetic field constrained by the Io flux tube footprint. J. Geophys. Res.: Space Physics 103, 11929–11939.

Cooper, J.F., Johnson, R.E., Mauk, B.H., Garrett, H.B., Gehrels, N., 2001. Energetic ion and electron irradiation of the icy Galilean satellites. Icarus 149, 133–159. https://doi.org/10.1006/icar.2000.6498.

Cunningham, N.J., Spencer, J.R., Feldman, P.D., Strobel, D.F., France, K., Osterman, S.N., 2015. Detection of Callisto's oxygen atmosphere with the Hubble space telescope. Icarus 254, 178–189. https://doi.org/10.1016/j.icarus.2015.03.021.

Dalton, J., Cassidy, T., Paranicas, C., Shirley, J., Prockter, L., Kamp, L., 2013. Exogenic controls on sulfuric acid hydrate production at the surface of Europa. Planet. Space Sci. 77, 45–63. https://doi.org/10.1016/j.pss.2012.05.013.

Divine, N., Garrett, H., 1983. Charged particle distributions in Jupiter's magnetosphere. J. Geophys. Res.: Space Phys. 88, 6889–6903.

Eviatar, A., Strobel, D.F., Wolven, B.C., Feldman, P.D., McGrath, M.A., Williams, D.J., 2001. Excitation of the Ganymede ultraviolet aurora. Astrophys. J. 555, 1013.

Fatemi, S., Poppe, A., Khurana, K., Holmström, M., Delory, G., 2016. On the formation of Ganymede's surface brightness asymmetries: kinetic simulations of Ganymede's magnetosphere. Geophys. Res. Lett. 43, 4745–4754. https://doi.org/10.1002/2016GL068363.

Feldman, P.D., McGrath, M.A., Strobel, D.F., Moos, H.W., Retherford, K.D., Wolven, B.C., 2000. HST/STIS ultraviolet imaging of polar aurora on Ganymede. Astrophys. J. 535, 1085.

Grasset, O., Dougherty, M., Coustenis, A., Bunce, E., Erd, C., Titov, D., Blanc, M., Coates, A., Drossart, P., Fletcher, L., Hussmann, H., Jaumann, R., Krupp, N., Lebreton, J.-P., Prieto-Ballesteros, O., Tortora, P., Tosi, F., Van Hoolst, T., 2013. JUpiter ICy moons Explorer (JUICE): an ESA mission to orbit Ganymede and to characterise the Jupiter system. Planet. Space Sci. 78, 1–21. https://doi.org/10.1016/j.pss.2012.12.002.

Gurnett, D.A., Persoon, A.M., Kurth, W.S., Roux, A., Bolton, S.J., 2000. Plasma densities in the vicinity of Callisto from Galileo plasma wave observations. Geophys. Res. Lett. 27, 1867–1870. https://doi.org/10.1029/2000GL003751.

Hall, D., Feldman, P., McGrath, M.A., Strobel, D., 1998. The far-ultraviolet oxygen airglow of Europa and Ganymede. Astrophys. J. 499, 475.

Hartkorn, O., Saur, J., 2017. Induction signals from Callisto's ionosphere and their implications on a possible subsurface ocean. J. Geophys. Res.: Space Physics 122, 11677–11697. https://doi.org/10.1002/2017JA024269.

Hartkorn, O., Saur, J., Strobel, D.F., 2017. Structure and density of Callisto's atmosphere from a fluid-kinetic model of its ionosphere: comparison with Hubble Space Telescope and Galileo observations. Icarus 282, 237–259. https://doi.org/10.1016/j.icarus.2016.09.020.

Hendrix, A.R., Johnson, R.E., 2008. Callisto: new insights from Galileo disk-resolved UV measurements. Astrophys. J. 687, 706.

Hibbitts, C., McCord, T., Hansen, G., 2000. Distributions of CO2 and SO2 on the surface of Callisto. J. Geophys. Res.: Plan 105, 22541–22557. https://doi.org/10.1029/1999JE001101.

Hill, T.W., 1979. Inertial limit on corotation. J. Geophys. Res. 84, 6554–6558. https://doi.org/10.1029/JA084iA11p06554.

Ip, W.-H., Williams, D., McEntire, R., Mauk, B., 1997. Energetic ion sputtering effects at Ganymede. Geophys. Res. Lett. 24, 2631–2634. https://doi.org/10.1029/97GL02814.

Ip, W.-H., Williams, D., McEntire, R., Mauk, B., 1998. Ion sputtering and surface erosion at Europa. Geophys. Res. Lett. 25, 829–832. https://doi.org/10.1029/98GL00472.

Johnson, T., Soderblom, L., Mosher, J., Danielson, G., Cook, A., Kupferman, P., 1983. Global multispectral mosaics of the icy Galilean satellites. J. Geophys. Res.: Solid Earth 88, 5789–5805. https://doi.org/10.1029/JB088iB07p05789.

Joy, S.P., Kivelson, M.G., Walker, R.J., Khurana, K.K., Russell, C.T., Ogino, T., 2002. Probabilistic models of the Jovian magnetopause and bow shock locations. J. Geophys. Res. (Space Phys.) 107, 1309. https://doi.org/10.1029/2001JA009146.

Khurana, K.K., 1997. Euler potential models of Jupiter's magnetospheric field. J. Geophys. Res. (Space Phys.) 102, 11295–11306. https://doi.org/10.1029/97JA00563.

Khurana, K.K., Kivelson, M.G., Stevenson, D.J., Schubert, G., Russell, C.T., Walker, R.J., Polanskey, C., 1998. Induced magnetic fields as evidence for subsurface oceans in Europa and Callisto. Nature 395, 777–780. https://doi.org/10.1038/27394.

Khurana, K.K., Russell, C.T., Dougherty, M.K., 2008. Magnetic portraits of tethys and Rhea. Icarus 193, 465–474. https://doi.org/10.1016/j.icarus.2007.08.005.

Kivelson, M.G., Bagenal, F., Kurth, W.S., Neubauer, F.M., Paranicas, C., Saur, J., 2004. Magnetospheric interactions with satellites. In: Bagenal, F., Dowling, T.E., McKinnon, W.B. (Eds.), Jupiter: the Planet, Satellites and Magnetosphere. Cambridge Univ. Press, pp. 513–536.

Kivelson, M.G., Khurana, K.K., Stevenson, D.J., Bennett, L., Joy, S., Russell, C.T., Walker, R.J., Zimmer, C., Polanskey, C., 1999. Europa and Callisto: induced or intrinsic fields in a periodically varying plasma environment. J. Geophys. Res. 104, 4609–4626. https://doi.org/10.1029/1998JA900095.

Kliore, A.J., Anabtawi, A., Herrera, R.G., Asmar, S.W., Nagy, A.F., Hinson, D.P., Flasar, F.M., 2002. Ionosphere of Callisto from Galileo radio occultation observations. J. Geophys. Res. (Space Phys.) 107, 1407. https://doi.org/10.1029/2002JA009365.

Kotova, A., Roussos, E., Krupp, N., Dandouras, I., 2015. Modeling of the energetic ion observations in the vicinity of Rhea and Dione. Icarus 258, 402–417. https://doi.org/10.1016/j.icarus.2015.06.031.

Krupp, N., Roussos, E., Kriegel, H., Kollmann, P., Kivelson, M.G., Kotova, A., Paranicas, C., Mitchell, D., Krimigis, S.M., Khurana, K.K., 2013. Energetic particle measurements in the vicinity of Dione during the three Cassini encounters 2005-2011. Icarus 226, 617–628. https://doi.org/10.1016/j.icarus.2013.06.007.

Kuskov, O.L., Kronrod, V.A., 2005. Models of the internal structure of Callisto. Sol. Syst. Res. 39, 283–301. https://doi.org/10.1007/s11208-005-0043-0.

Liuzzo, L., Feyerabend, M., Simon, S., Motschmann, U., 2015. The impact of Callisto's atmosphere on its plasma interaction with the Jovian magnetosphere. J. Geophys. Res. (Space Phys.) 120, 9401–9427. https://doi.org/10.1002/2015JA021792.

Liuzzo, L., Simon, S., Feyerabend, M., 2018. Observability of Callisto's inductive signature during the JUpiter ICy moons Explorer mission. J. Geophys. Res.: Space Phys. 123, 9045–9054. https://doi.org/10.1029/2018JA025951.

Liuzzo, L., Simon, S., Feyerabend, M., Motschmann, U., 2016. Disentangling plasma interaction and induction signatures at Callisto: the Galileo C10 flyby. J. Geophys. Res.: Space Phys. 121, 8677–8694. https://doi.org/10.1002/2016JA023236.

Liuzzo, L., Simon, S., Feyerabend, M., Motschmann, U., 2017. Magnetic signatures of plasma interaction and induction at Callisto: the Galileo C21, C22, C23, and C30 flybys. J. Geophys. Res.: Space Phys. 122, 7364–7386. https://doi.org/10.1002/2017JA024303.

Liuzzo, L., Simon, S., Regoli, L., 2019. Energetic ion dynamics near Callisto. Planet. Space Sci. 166, 23–53. https://doi.org/10.1016/j.pss.2018.07.014.

Matsumoto, H., Omura, Y., 1985. Particle simulation of electromagnetic waves and its application to space plasmas. Comput. Simulat. Space Plasmas 43.

Mauk, B., Mitchell, D., McEntire, R., Paranicas, C., Roelof, E., Williams, D., Krimigis, S., Lagg, A., 2004. Energetic ion characteristics and neutral gas interactions in Jupiter's magnetosphere. J. Geophys. Res.: Space Phys. 109 https://doi.org/10.1029/2003JA010270.

Mauk, B.H., Saur, J., 2007. Equatorial electron beams and auroral structuring at Jupiter. J. Geophys. Res.: Space Phys. 112.

McEwen, A.S., 1986. Exogenic and endogenic albedo and color patterns on Europa. J. Geophys. Res.: Solid Earth 91, 8077–8097. https://doi.org/10.1029/JB091iB08p08077.

McGrath, M.A., Jia, X., Retherford, K., Feldman, P.D., Strobel, D.F., Saur, J., 2013. Aurora on Ganymede. J. Geophys. Res.: Space Phys. 118, 2043–2054. https://doi.org/10.1002/jgra.50122.

Mueller, S., McKinnon, W.B., 1988. Three-layered models of Ganymede and Callisto - compositions, structures, and aspects of evolution. Icarus 76, 437–464. https://doi.org/10.1016/0019-1035(88)90014-0.

Müller, J., Simon, S., Motschmann, U., Schüle, J., Glassmeier, K., Pringle, G.J., 2011. A.I.K.E.F.: Adaptive hybrid model for space plasma simulations. Comput. Phys. Commun. 182, 946–966. https://doi.org/10.1016/j.cpc.2010.12.033.

Neubauer, F.M., 1980. Nonlinear standing Alfvén wave current system at Io: Theory. J. Geophys. Res. (Space Phys.) 85, 1171–1178. https://doi.org/10.1029/JA085iA03p01171.

Neubauer, F.M., 1998. The sub-Alfvénic interaction of the Galilean satellites with the Jovian magnetosphere. J. Geophys. Res. (Space Phys.) 103, 19843–19866. https://doi.org/10.1029/97JE03370.

Nordheim, T., Hand, K., Paranicas, C., 2018. Preservation of potential biosignatures in the shallow subsurface of Europa. Nature Astronomy 2, 673. https://doi.org/10.1038/s41550-018-0499-8.

Paranicas, C., Carlson, R., Johnson, R., 2001. Electron bombardment of Europa. Geophys. Res. Lett. 28, 673–676. https://doi.org/10.1029/2000GL012320.

Paranicas, C., Hibbitts, C., Kollmann, P., Ligier, N., Hendrix, A., Nordheim, T., Roussos, E., Krupp, N., Blaney, D., Cassidy, T., Clark, G., 2018. Magnetospheric considerations for solar system ice state. Icarus 302, 560–564. https://doi.org/10.1016/j.icarus.2017.12.013.

Paranicas, C., McEntire, R., Cheng, A., Lagg, A., Williams, D., 2000. Energetic charged particles near Europa. J. Geophys. Res.: Space Phys. 105, 16005–16015. https://doi.org/10.1029/1999JA000350.

Plainaki, C., Milillo, A., Mura, A., Saur, J., Orsini, S., Massetti, S., 2013. Exospheric O2 densities at Europa during different orbital phases. Planet. Space Sci. 88, 42–52. https://doi.org/10.1016/j.pss.2013.08.011.

Poppe, A., Fatemi, S., Khurana, K., 2018. Thermal and energetic ion dynamics in Ganymede's magnetosphere. J. Geophys. Res.: Space Phys. https://doi.org/10.1029/2018JA025312.

Regoli, L., Roussos, E., Feyerabend, M., Jones, G.H., Krupp, N., Coates, A.J., Simon, S., Motschmann, U., Dougherty, M., 2016. Access of energetic particles to Titan's exobase: a study of Cassini's T9 flyby. Planet. Space Sci. 130, 40–53. https://doi.org/10.1016/j.pss.2015.11.013.

Roederer, J.G., 1967. On the adiabatic motion of energetic particles in a model magnetosphere. J. Geophys. Res. 72, 981–992. https://doi.org/10.1029/JZ072i003p00981.

Roussos, E., Kollmann, P., Krupp, N., Paranicas, C., Krimigis, S., Mitchell, D., Persoon, A., Gurnett, D., Kurth, W., Kriegel, H., et al., 2012. Energetic electron observations of Rhea's magnetospheric interaction. Icarus 221, 116–134. https://doi.org/10.1016/j.icarus.2012.07.006.

Seufert, M., Saur, J., Neubauer, F.M., 2011. Multi-frequency electromagnetic sounding of the Galilean mo. Icarus 214, 477–494. https://doi.org/10.1016/j.icarus.2011.03.017.

Snowden, D., Yelle, R., 2014. The global precipitation of magnetospheric electrons into Titan's upper atmosphere. Icarus 243, 1–15.

Snowden, D., Yelle, R., Galand, M., Coates, A.J., Wellbrock, A., Jones, G.H., Lavvas, P., 2013. Auroral electron precipitation and flux tube erosion in Titan's upper atmosphere. Icarus 226, 186–204.

Spencer, J.R., 1987. Thermal segregation of water ice on the Galilean satellites. Icarus 69, 297–313. https://doi.org/10.1016/0019-1035(87)90107-2.

Vay, J.-L., 2008. Simulation of beams or plasmas crossing at relativistic velocity. Phys. Plasmas 15, 056701.

Vorburger, A., Wurz, P., 2018. Europa's ice-related atmosphere: the sputter contribution. Icarus 311, 135–145. https://doi.org/10.1016/j.icarus.2018.03.022.

Vorburger, A., Wurz, P., Lammer, H., Barabash, S., Mousis, O., 2015. Monte-Carlo simulation of Callisto's exosphere. Icarus 262, 14–29. https://doi.org/10.1016/j.icarus.2015.07.035.

Williams, D., McEntire, R., Jaskulek, S., Wilken, B., 1992. The Galileo energetic particles detector. Space Sci. Rev. 60, 385–412. https://doi.org/10.1007/BF00216863.

Zimmer, C., Khurana, K.K., Kivelson, M.G., 2000. Subsurface oceans on Europa and Callisto: constraints from Galileo magnetometer observations. Icarus 147, 329–347. https://doi.org/10.1006/icar.2000.6456.